Chapter III

Pristine NiMOF sandwiched between 1D and 3D engineered Au-particles and dendritic platform for ultra-swift folic acid sensing in cellular microenvironment

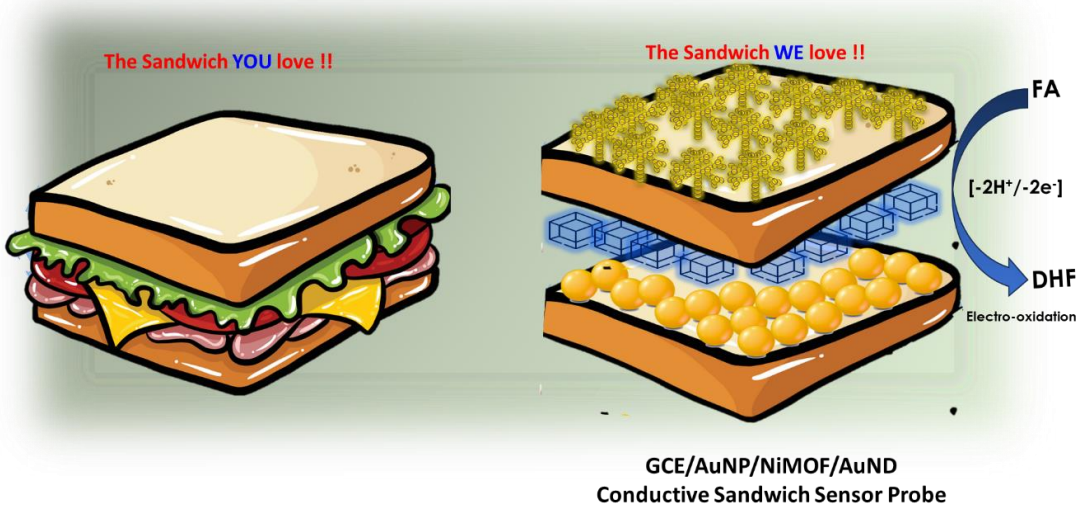

Shubhangi et al., ACS Analytical Chemistry, 2024 (In Press: 10.1021/acs.analchem.4c03564)

1. Introduction

Folic acid (FA), a common name for pteroylglutamic acid, is an essential water-soluble vitamin (Vit. B9) of the B-complex category. Its primary essentiality revolves around important bodily functions like being precursor for various coenzymes such as ferroheme, synthesis of purines and pyrimidines and thereby, vital role in the fixing, methylation and synthesis of DNA[1,2]. It is a synthetic substitute of Vit. B9 or folacin which is chemically (2S)-2-[[4-[(2-amino-4-oxo-1Hpteridin- 6-yl)methylamino]benzoyl]amino] pentanedioic acid. It gained its prominence in the beginning of the century as the understanding on its deficiency grew[3,4]. A decrease in its body fluid concentration ($34.4 \pm 10.4\ 10^{-9}$ M) has found its linkage to various diseases such as mental deconvolution, leucopoenia, gigantocytic anaemia and increased possibilities for heart attacks and cancer[5]. While its supplementation reduces the occurrence of neural tube defects such as spinal bifida in women as well as carcinogenesis due to its involvement in nucleotide synthesis, the over-expression of its receptors on cancerous cells makes its receptors as classic tumour markers due to the cells' risen metabolic FA uptake[6–8]. There have been conflicting reports on its role in suppressing as well as increasing carcinogenesis in clinical subjects with varying clinical diagnosis[9–11]. This makes its judicious supplementation and quantitative detection through selective and sensitive sensing modules the need of the hour. Whilst it is naturally synthesized in green leafy plants, algae and microbes such as yeast and bacteria, its deficiency is coped up in humans through dietary or pharmaceutical supplementation[12].

FA detection has been practiced through various methods including the traditional spectrophotometry[13], colorimetry[14], mass spectroscopy[15], electrophoretic[16] methods along with sophisticated methods like high performance liquid chromatography[17], flow injection chemiluminescence[18], ELISA [19] and many others. The major drawback of these

methods is that they require expensive setups, expertise in operations and are time-consuming. To overcome these challenges, newer and more sensitive tools such as electrochemical methods have been introduced into the domain of FA sensing which has not only revolutionized the sensing arena by reducing costs and time but also improved the sensor efficacy in terms of FA sensitivity and LOD[2]. Nanostructured materials with varying compositions and functionalities have garnered immense interest in recent times for electrochemical sensing module development[20]. Nanomaterials of different sizes, electronic properties and surface characteristics can be clubbed together through probe surface nano-engineering to develop novel sensing matrices of desirable functionalities[21].

MOFs are an emerging class of crystalline porous materials which have transcended their potential in electrochemical sensing roles[22]. Their catalytic metal centres self-assembled with organic ligands offer opportunities for surface functionalization, chemical and non-chemical molecular adhesions and large surface area paving their functional potential in sensing[23]. In regards to their explored roles as FA sensing modules, they have mostly been adopted in optical sensor matrices with rare earth metal centres having their own set of limitations such as high fabrication time and low selectivity[24]. Conversely, MOF synthesized through the solvothermal synthesis route exhibit poor conductivity in electrochemical sensing due to organic solvent interventions. Switching towards electrochemical MOF synthesis for development of electrochemical sensors could be a pivotal step to surpass the hurdles dealt in this route so far.

3D nanomaterials such as metallic nanodendrites are architecturally remarkable structures comprising of branched stems, possessing commendable conductivity[25]. Since being from metallic origin, AuND outperform several other 3D materials in their catalytic potential due to presence of enormous active sites[26]. 1D AuNPs are also widely employed in sensing due to their observable electrical, and catalytic capabilities, in addition to their

possible functionalization on surfaces[27]. Thus, we hypothesize that a composite system comprising AuND and AuNP with MOF can accentuate the surface charge transfer characteristics by many folds due to the amalgamation of two highly catalytic and conductive surfaces.

In view of this, we have attempted fabrication of a sandwich-like unique GCE/AuNP/NiMOF/AuND sensing platform for the sensitive detection of FA in serum and *in vitro* cellular microenvironment. The probe matrix surface has been initially characterized through scanning probe microscopy (SPM), scanning electron microscopy (SEM), energy dispersive X-ray analysis (EDX-mapping) and Fourier transform infrared (FTIR) analysis followed by electrochemical studies. The electrochemical studies have initially been deployed for the characterization of the metal centres of the sensor probe, followed by understanding each fabricated layer and their roles in sensing. All experiments have been cross-referenced through a set of control experiments, followed by deducing tangible outcomes in terms of LOD, LDR, response time, selectivity, and sensitivity of the probe. The results have been complemented with tabular entries for comparing the developed probe with existing ones. This study is one of its kind, where a simple and highly functional catalytic system has been developed to detect FA in clinical ranges and much beyond. It is worth mentioning that the developed sensing assembly is an amalgamation of materials of all three dimensions (1D, 2D and 3D), leveraging property from each one of them for cumulative outcome.

The **Figure 3.1** illustrates the fabrication of a sandwich model comprising NiMOF layered between AuNPs and AuNDs, its possible role in FA oxidation, and its deployment in real-time FA sensing in MCF-7 cell lines.

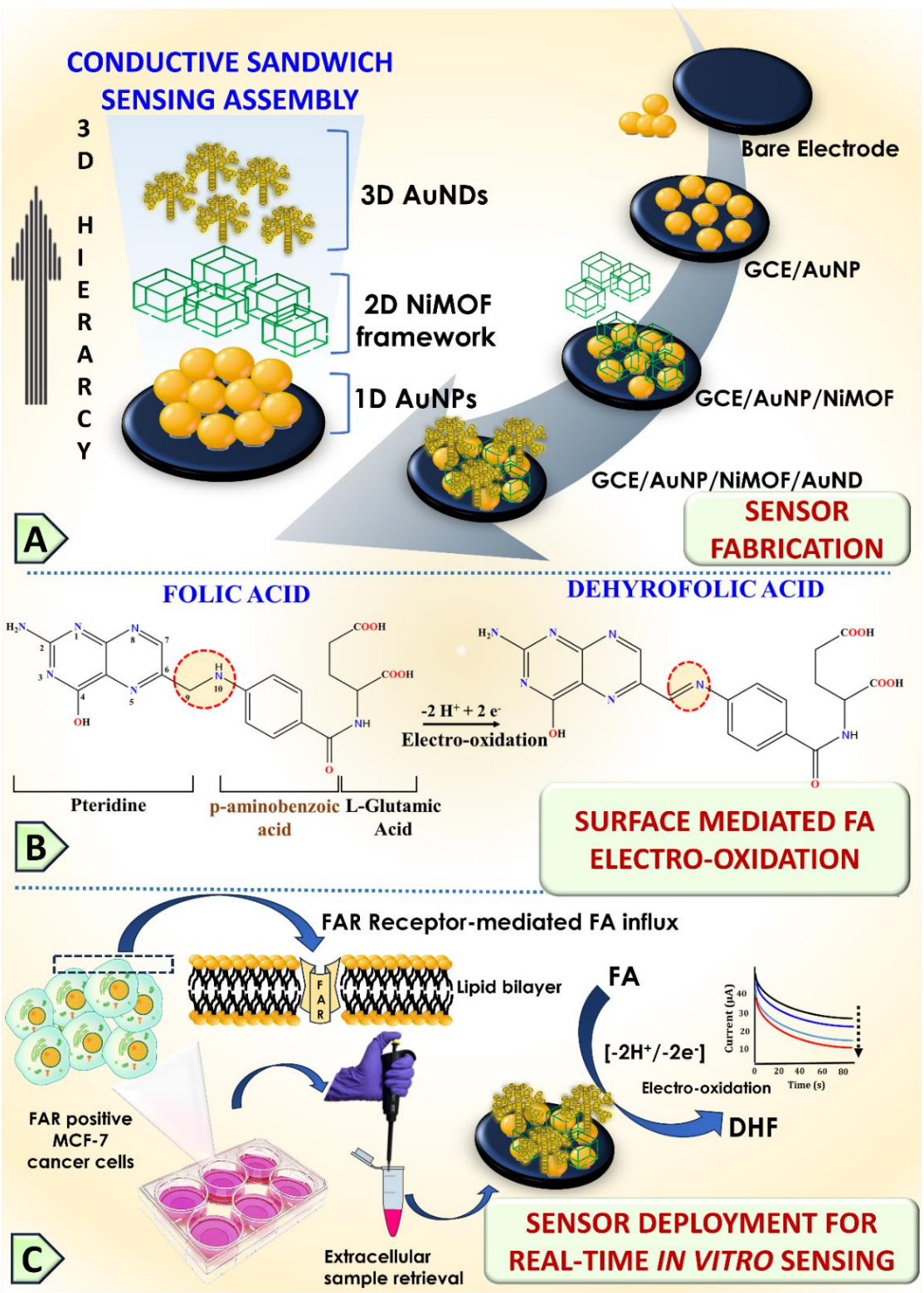

Figure 3.1. *The panel (A) showcases the fabrication steps involved for the development of GCE/AuNP/NiMOF/AuND; (B) the proposed mechanism behind electro-oxidative conversion of FA; and (C) overall strategy for deployment of the developed sensor involving the cancer cellular microenvironment.*

2. Materials and Methods

2.1. Chemicals and Instruments

All chemicals and reagents used in different sets of experiments in this work were of the analytical grade. ZoBell's electrolytic solution (ZS) ($K_3[Fe(CN)_6]/K_4[Fe(CN)_6]$), 5mM; pH-7) was prepared using potassium hexacyanoferrate (II) ($K_4Fe(CN)_6$) and potassium hexacyanoferrate (III) ($K_3Fe(CN)_6$), procured from Himedia Pvt. Ltd., Mumbai, India. Phosphate-buffered saline (PBS, pH-7) was made in-house using sodium monophosphate (NaH_2PO_4), sodium bisphosphate (Na_2HPO_4), and sodium chloride (NaCl), bought from Sisco Research Pvt. Ltd. (SRL), India. Potassium chloride (KCl), chloroauric acid ($HAuCl_4.3H_2O$), and sulphuric acid (H_2SO_4) were utilized for synthesizing AuNP and AuND precursor solutions, which were procured from SRL, India. Dimethyl formamide (DMF), nickel nitrate hexahydrate ($Ni(NO_3)_2.6H_2O$), and 2 methyl-imidazole(Me-Im) were used for the fabrication of the NiMOF, which were all procured from SRL, India. FA was obtained from Sigma-Aldrich Chemical Co. (India). Double-distilled water from a Milli-Q water purifier (water resistance 18.2 MΩ) was used for the preparation of standard solutions. MCF-7 cell line (breast cancer cells) was procured from NCCS, Pune. Dulbecco's modified Eagle's medium (DMEM) was purchased from Himedia (AL007F), fetal bovine serum (FBS) was bought from Gibco (10270106), PBS was purchased for cell culture experiments from Sigma-Aldrich (D5652-10L) while the Pen-Strep and 6-well plates were procured from Edna BioLabs (PENSTRP-100) and SPL life sciences (30006), respectively.

All physical characterizations were carried out at the Central Instrument Facility Centre (CIFC), IIT (BHU). SPM was performed using NTEGRA Prima by NT-MDT Service & Logistics Ltd., HR-SEM using Nova Nano SEM 450 by FEI, EDS by EDAX Inc. and FTIR using Nicolet iS5 by the Thermo Electron Scientific Instruments LLC. For all the

electrochemical measurements, an electrochemical workstation (Palm Sens 4.0, Houten, Netherlands) was deployed. It comprised of a three-electrode system with Ag/AgCl as the reference, Pt wire as the counter and glassy carbon electrode (GCE) as the working electrode in the current set of experiments.

2.2. GCE/AuNP/NiMOF/AuND sensor probe fabrication

Bare GCE surface was polished and pre-treated as per the standard procedure to clean all surface impurities[26]. The foremost layer comprising of AuNPs was electrodeposited onto the GCE surface through linear sweep voltammetry (LSV). The pretreatment parameters were optimized as -0.6 V vs. Ag/AgCl, 60 s, where cleaned GCE was dipped into a 0.5 M H_2SO_4 AuNP precursor solution containing 0.001% $HAuCl_4.3H_2O$. Further, the consecutive layer comprising of NiMOF was fabricated over GCE/AuNP through an electrochemical approach using chronoamperometry (CA) at a potential of -1.4 V vs. Ag/AgCl for 300 s. The MOF precursor solution contained 50 mM $Ni(NO_3)_2.6H_2O$ and 75 mM of 2-MeIm in 10 ml DMF solvent system, which was stirred for 10 minutes before the electrodeposition step. The obtained GCE/AuNP/NiMOF probe was rinsed with Milli-Q water and then further electrocoated with the topmost layer of AuNDs. The synthesis of AuNDs was optimized to devise the final deposition conditions as -0.3 V vs. Ag/AgCl, 1500 s, using a 10 mM $HAuCl_4.3H_2O$ solution, that was dissolved in 0.1 M KCl solution. The final sensing probe, GCE/AuNP/NiMOF/AuND, was then subjected to a set of physical and electrochemical characterizations before use for the purpose of FA sensing. A series of control experiments were performed to confirm the presence and importance of each matrix component in the final sensing assembly. The validation of Au was done through dipping the GCE/AuNP/NiMOF/AuND sensor probe in 0.5 M H_2SO_4, while the estimation of Ni metal was done by dipping the same into 0.1 M NaOH in a separate experimental setting. For all physical characterizations, each layer was

individually developed and tested for comparative and critical examination. On completion of the final GCE/AuNP/NiMOF/AuND probe fabrication, it was double rinsed with Milli-Q water each time, dried at room temperature (RT), and stored in a desiccator for further usage.

2.3. Electrochemical characterization of GCE/AuNP/NiMOF/AuND sensor probe

The first step towards verification of the fabricated GCE/AuNP/NiMOF/AuND sensor probe was through its electrochemical characterization in ZS (pH=7). CV and EIS techniques were adopted for the characterization purposes using the three-electrode setup. EIS data recording was done at the rate of ten points per decade sampling, keeping the open circuit voltage within 10 to 104 Hz. The control studies were performed through DPV followed by recording the calibration responses through CA at a potential of +0.8 V vs. Ag/AgCl for 100 s.

2.4. Real Sample Analysis

2.4.1. Sensor Validation in Serum samples

The applicability of the developed GCE/AuNP/NiMOF/AuND sensing probe was initially validated on serum samples through the standard method of spike and recovery. In this method, the obtained serum was spiked with different concentrations of FA after initial 10x dilution with 0.1 M PBS. The rationale behind dilution of serum samples is to maintain the molar strength of the real matrix for the better understanding of the sensor performance. The recorded output current was plotted and compared to the standard calibration curve to study the FA concentration-dependent studies in a real matrix like serum.

2.4.2. In vitro sensing and real-time FA uptake in cellular microenvironment

MCF-7 cells were cultured in folate-free DMEM supplemented with 10% FBS and 1% penicillin/streptomycin in 6-well plates. Each well was filled with 1.5 ml of folate-free media. Cultures were maintained under standard conditions at 37°C with 5% CO2 purging and 95% humidity. Cell growth was regularly observed using microscopic examination. Upon reaching 90% confluency, 150 µl of FA dissolved in PBS was added to each well, resulting in a final concentration of 10-4 M FA. Cell growth medium was collected at every 3-hour intervals starting from t=0 until t=24, encompassing a total of 7 time points. Duplicate wells were prepared for each time point, and corresponding media control was set up, where only media and FA were added without the cells. The collected samples were analyzed, post 1/10 dilution in the PBS buffer, using the FA sensor and compared with the control wells, where no FA was added.

3. Results and Discussion

3.1. Electrochemical surface engineering and characterization of GCE/AuNP/Ni MOF/AuND sensor probe

Several sets of probe optimization-driven approach were adopted to fabricate the sensor probe. The GCE working electrode was fabricated by electrocoating it with three consecutive layers of AuNPs, NiMOF, and AuNDs to obtain the final GCE/AuNP/NiMOF/AuND sensor probe surface. Various physical and electrochemical characterization experiments were performed to confirm the presence of constituting elements and conductive layers, as discussed in the upcoming sections.

Physical Characterizations

3.1.1. SPM studies

SPM can be a powerful tool to understand the overall surface topology and individual layer thickness. A tapping mode study was conducted on each electrodeposited surface fabricated on a clean electrode. The probe and cantilever specifications can be referred to in detail within **'Additional Information'** section within a box on the page. The bare electrode surface (referred as WE in **Figure 3.2**) exhibits an evenly distributed pitch of analysis, with the adjoining 2D micrograph stating an average z-deflection of 5.42 nm (**Figure 3.2A**). Upon deposition of the AuNPs as the first layer onto the bare WE, a rise in the crest thickness throughout the surface was seen with an average z-deflection of 12.53 nm, as evident from **Figure 3.2B**. An even deposition of AuNPs can be inferred from the graph. On further surface modification using NiMOF, the sharpness in peaks is drastically reduced, with enlargement in crests and a significant change in surface topology, and they possess an average z-deflection of 28.40 nm. This could be due to successful fabrication of electrodeposited NiMOF embedded over the

Additional Information: Details on the SPM Cantilever Specifications

Model: NTEGRA Prima; **Company:** NT-MDT Service & Logistics Ltd.

Characterization was performed through a Noncontact Polysilicone probe, tip material comprised of silicon with cantilever chip size being 1.6 x 3.6 mm and thickness of 0.45 mm. The curvature radius of the tip was around 10 mm. The cantilever specifications were as follows:

- Cantilever length (in µm): 94 with a typical dispersion of about ± 2
- Cantilever width (in µm): 34 with a typical dispersion of about ± 3
- Cantilever thickness (in µm): 1,85 with a typical dispersion of about ± 0.15
- Force Constant (N/m) = 12 with a typical dispersion of about ± 20%
- Resonant Frequency (kHz) = 235 with a typical dispersion of ± 10%.

AuNPs (**Figure 3.2C**). This was followed by the deposition of the final dendritic layer onto the WE/AuNP/NiMOF surface. The uniformity of the probe was restored with a further increment in the z-deflection to 219.43 nm (**Figure 3.2D**). The SPM study was critically evaluated on the basis of the relative rise in the z-deflection values on successive depositions, as also stated in the respective 2D micrographs. The micrographs were obtained at different magnifications, depicting similarity in outcomes and establishing the notion of uniform layer fabrication at each step. The certainty of individual nanostructures and the chemical insights of those nanostructures were established by further studies like SEM, EDX, and FTIR analyses.

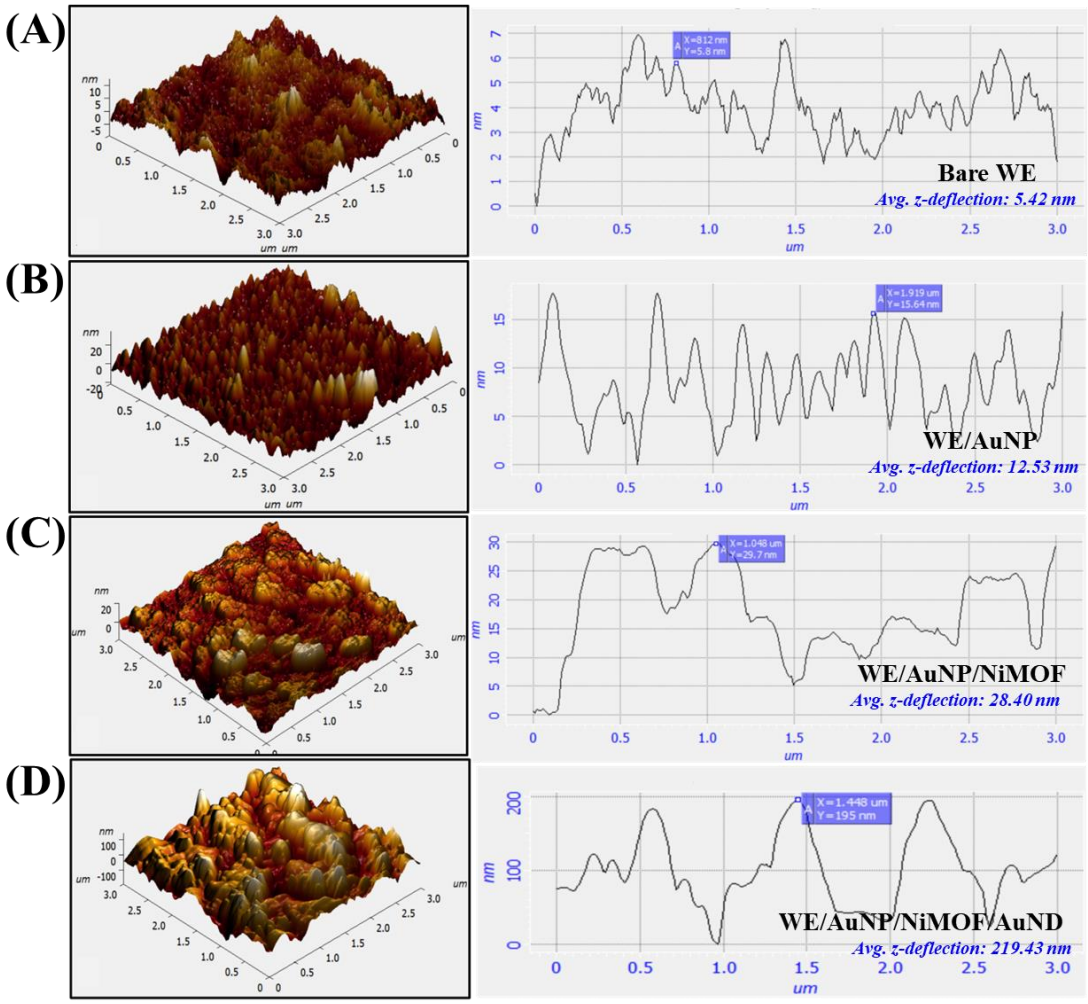

Figure 3.2. *SPM 3D and the corresponding 2D micrographs for **A)** bare WE; **B)** first thin film deposited, viz., WE/AuNPs; **C)** the second electrodeposited film of WE/AuNPs/NiMOF; **D)** the final film of WE/AuNPs/NiMOF/AuND.*

3.1.2. SEM and EDX analysis

The immaculate nanostructural morphology of the sensing probe was analysed through SEM. A clean electrode surface was taken to nanoimprint AuNP onto it, followed with subsequent modification by electrodeposited NiMOF to obtain WE/AuNP/NiMOF probe surface. **Figure 3.3A** depicts the dense clusters of NiMOF grown over the surface of AuNPs[23]. The cabbage-like morphology of the composite is a classical outcome seen in electrodeposited MOFs[28]. The encircled regions in yellow have been further zoomed-in within the image as 'insets' to understand the morphology on subsequent degree of magnifications. On further modifying the WE/AuNP/NiMOF with AuNDs, the imprinted nanodendritic structures can be seen intercalated between NiMOF clusters. A uniform distribution of AuNDs throughout the analysis pitch can be seen, which has been more clearly demarcated in red dotted circles (**Figure 3.3B)**. Yellow circles still visible in the area refer to the WE/AuNP/NiMOF clusters uncovered with AuNDs. The **inset of Figure 3.3B** shows an enlarged view of one such AuND with a primary (1°) branch/central rib (denoted in light yellow dotted line), secondary (2°) branch (denoted in pink dotted lines), and, in some cases, tertiary (3°) branches (specified through orange dotted lines). The 1° branch splits into the subordinating branches to mimic an established fern-like morphology of the AuNDs. To understand the morphology of each layer more lucidly, an individual layer of the probe was fabricated on the bare WE surface and analysed under SEM (as depicted in **Figure 3.3** 'C', 'D', and 'E' corresponding to AuNP, NiMOF, and AuND, respectively).

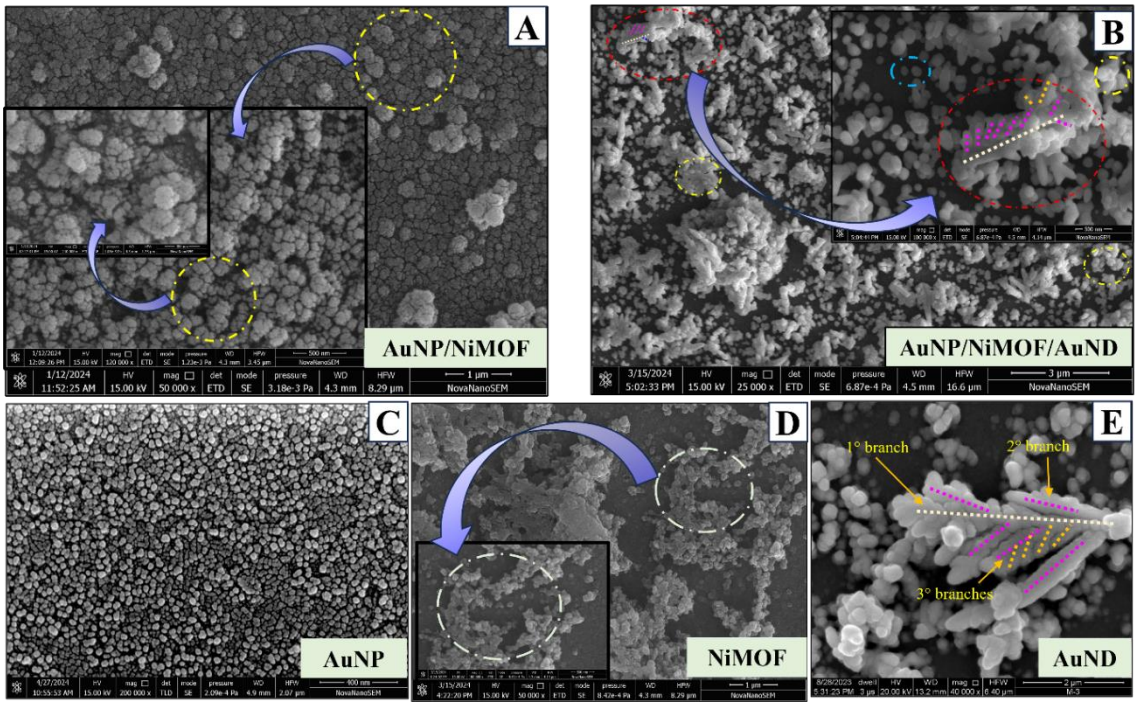

Figure 3.3. *SEM micrographs of (A) WE/AuNP/NiMOF; (B) WE/AuNP/NiMOF/AuND; (C) electrodeposited AuNP; (D) electrodeposited NiMOF; and (E) electrodeposited AuND on electrode surface.*

For the further validation of the elemental composition of constituents, the WE/AuNP/NiMOF/AuND sensor probe was subjected to elemental mapping coupled with EDX analysis. The obtained results have been represented in **Figure 3.4,** where the **Figure 3.4A(a)** is the actual area under scan. It is to note that the mapped results have been discussed with an assumption that similar and equal distribution of electrodeposited structures are present throughout the pitch of the electrode. **Figure 3.4A(b)** demonstrates the cumulative micrograph of all elements, viz., C (**Figure 3.4B-i**), N (**Figure 3.4B-ii**), Ni (**Figure 3.4B-iii**), and Au (**Figure 3.4B-iv**), illustrated through **green, yellow, orange,** and **brown-colored** patterns**,** respectively. The segregation into constituent elemental micrographs has been depicted for lucid understanding of the reader. The EDX analysis of the demarcated area in red **(Figure 3.4C)** confirms the presence of C, N, Ni, and Au elements in the atomic percentage of about 14.77%, 20.34%, 14.68%, and 32.24 %, respectively. We have reconfirmed these elements from the electrochemical methods in further section ahead. To reconfirm the presence of NiMOF onto the electrode surface,

FTIR analysis of NiMOF coated electrode surface was done, which confirmed peaks corresponding to desirable functional groups, re-affirming our notion on MOF synthesis.

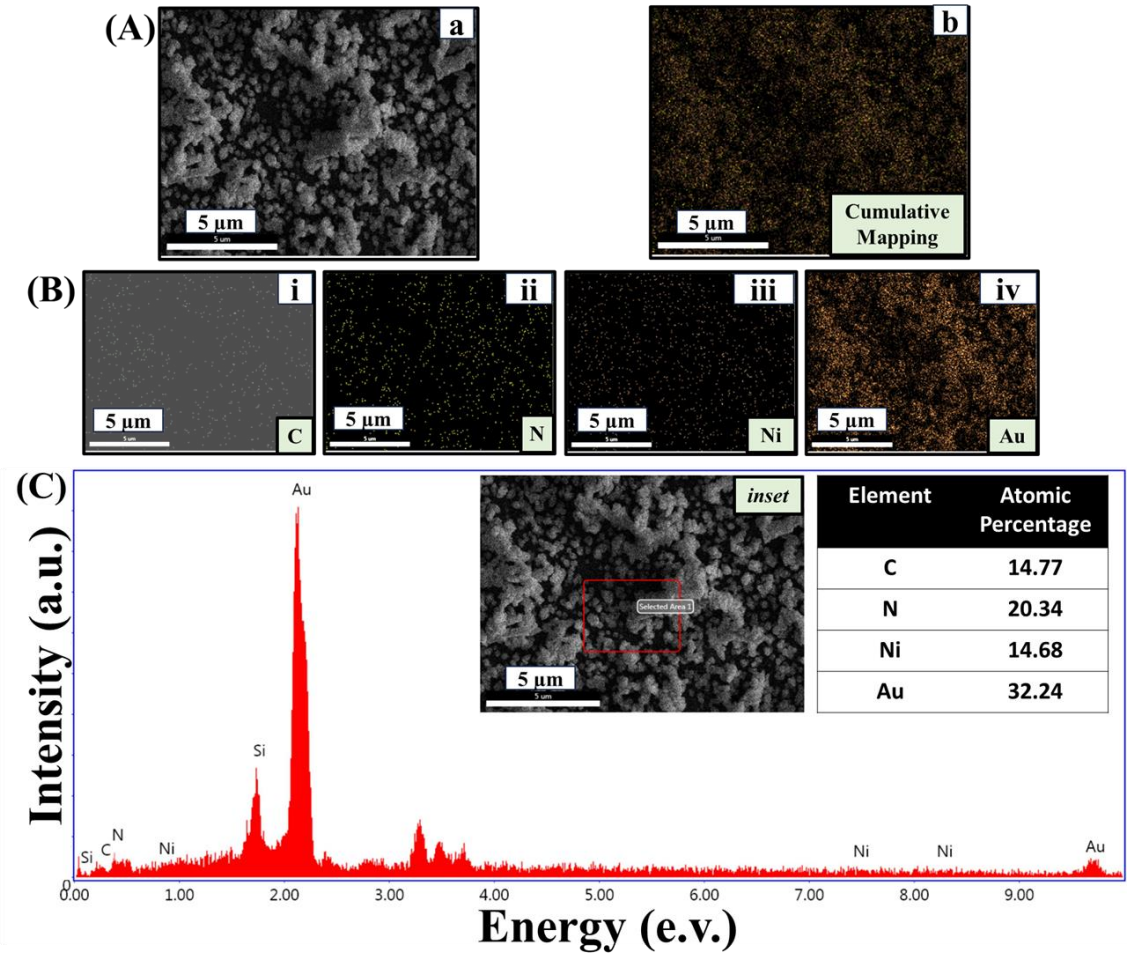

Figure 3.4. *The EDX mapping results for the wide area under investigation stated in A(a), with a cumulative mapping result in A(b), which has further been dissociated into individual elemental compositions micrographs of the surface where, (B-i) corresponds to 'C'; (B-ii) corresponds to 'N'; (B-iii) corresponds to 'Ni', and (B-iv) corresponds to Au. The mapped results have been further complemented with elemental table of constituting elements, as shown in tabulated form in (C) part.*

3.1.3. FTIR analysis for NiMOF

The FTIR spectrum was obtained to analyse present functional groups in a wide wavelength range of 4000-450 cm^{-1}. The spectrum presented with corresponding peaks confirm the desirable functional groups and thereby successful electro-synthesis of NiMOF through the novel route[23]. The bending and stretching vibrations of the imidazole ring, part of the linker moiety, were prominent in the region of 450-1640 cm^{-1} [29]. Two

doublet peaks were observed in the range of 692-717 cm^{-1} belonging to the C-H stretching bonds present in the methyl group of the linker. A classic peak at around 474 cm^{-1} corresponds to Ni-N bond, which establishes the notion for successful NiMOF formation[29]. Apart from this, the C-N, C=N, and alkene C=C stretching vibrations in the linker contributes to a peak at around 1200, 1445, 1640 cm^{-1}. Apart from this, the -OH stretching vibration at 3439 cm^{-1} corresponds to the moisture as well as hydroxyl moieties present in the MOF structure. Two peaks located at 2856 and 2932 cm^{-1} correspond to =C-H bond vibrations from the aromatic and aliphatic rings in the imidazole structure. The FTIR, SEM and EDX-mapping results cumulatively confirm the formation, morphology, as well as composition of the final sensing matrix's constituents.

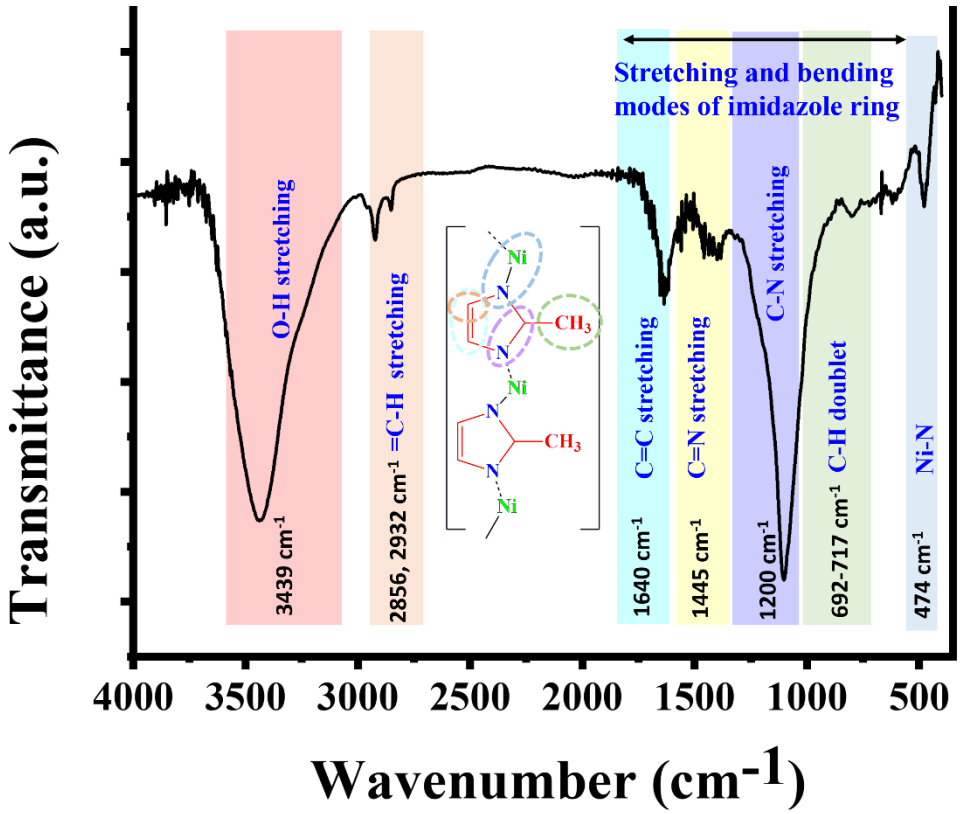

Figure 3.5. *FTIR analysis for NiMOF formation*

The physical characterisation results were verified through a series of electrochemical experiments as discussed in further sections below.

3.1.4. Catalytic metal elemental validation on the GCE/AuNP/NiMOF/AuND probe surface

The presence of Au in the electrodeposited AuNPs as well as AuNDs, along with the Ni metal centre validation in the NiMOF, on the developed sensor surface were verified through a set of separate experiments and controls on the same electrode in different electrolytes. At the first stage, the initial layer comprising of GCE/AuNP was fabricated and then, scanned within a potential range of +0.4 V to +1.6 V vs. Ag/AgCl in a 0.5 M H_2SO_4 solution to estimate the presence of Au in the fabricated nanostructures. A characteristic 'Au' peak was noted in lieu of, in accordance to the electrochemical behavior of the deposited gold in its reduced form as AuNPs on the probe surface, at +0.9 V vs. Ag/AgCl (**Figure 3.6A-i)**. A feeble peak around +1.3 V vs. Ag/AgCl was also seen however was lesser prominent in the case. Then, the same electrode was subjected to further modification through the electrochemical synthesis of the NiMOF. It was then, dipped into a solution containing 0.1 M NaOH and scanned within a potential window of -0.5 V to +0.5 V vs. Ag/AgCl. A characteristic Ni oxidation peak was observed at +0.3 V vs. Ag/AgCl **(Figure 3.6B-i),** which was not seen earlier while scanning a bare GCE probe in the same potential window. This affirmed the Ni^{+2} presence exclusively post electrodeposition of the NiMOF onto the probe. The final step involving the electrodeposition of the AuNDs was carried out on the surface post Ni estimation. The probe was then, re-immersed into the 0.5 M H_2SO_4 solution, and scanned within the potential window of +0.6 V to +1.2 V vs. Ag/AgCl. There was a significant enhancement in the characteristic peak intensities at +0.9 V vs. Ag/AgCl as well as at +1.2 V vs. Ag/AgCl (which was earlier not that prominent), suggestive of presence of more Au-based deposition on the probe surface **(Figure 3.6C-i)**. From this significant rise in Au redox signals, it can be inferred that clusters of AuND are forming on the sensor surface

leading to this rise. To eliminate even a modicum of doubt, a negative control study was done, where an unmodified GCE was tested in similar settings, yielding no results in that case. The stability of the individual probe layers and electron transfer mechanisms were validated through a scan rate study as well. The cathodic (Ipc) and anodic (Ipa) peak currents were found directly proportional to the scan rates, with the correlation coefficient values corresponding to 0.99 and 0.99 for Au in AuNPs, 0.97 for Ni, and 0.99 and 0.99 for Au in AuNDs, respectively. This demonstrates the stable surface adsorption/adhesion phenomena with stability even at higher scan rates, making the engineered probe ideal for real sample sensing modules as well. Thus, the set of physical and electrochemical characterization studies conclusively validated the presence, composition and overall morphology of the constituting metallic nanostructures in the final GCE/AuNP/NiMOF/AuND sensing probe.

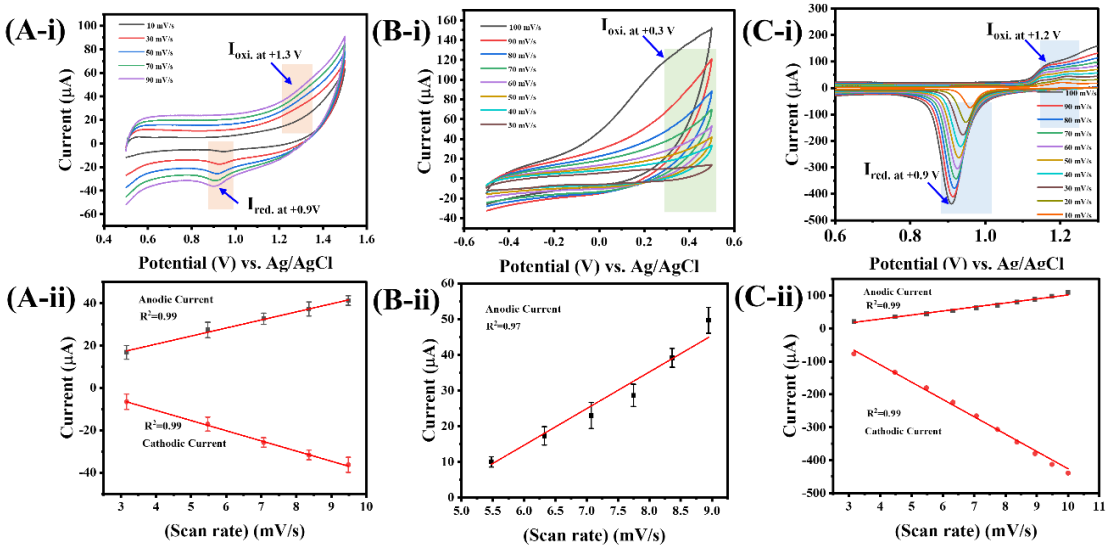

Figure 3.6. *Electrochemical estimation of probe elements where A-i and A-ii correspond to the redox and fitting curves for AuNPs, B-i and B-ii refer to the oxidation and fitting curves for Ni metal of the NiMOF, and similarly, C-i and C-ii correspond to redox peak and fitting curves for the Au metal of the AuND component within the final sensing matrix.*

3.2. Electrochemical performance of GCE/AuNP/NiMOF/AuND sensor probe

After verifying the presence of desirable metals in the sensor, it was time to proceed with the electrochemical examination to check its electron transfer and electrocatalytic

potential. For this purpose, CV was conducted in ZS solution at RT within an analysis window of -0.1 V to +0.5 V vs. Ag/AgCl at a scan rate of 50 mV/s (n=5). The peaks observed within the set window were observed in all cases (including the bare GCE surface**, red curve**), due to the inherent known redox behavior of ZS. Peaks corresponding to GCE/AuNPs (**black curve**), GCE/AuNP/NiMOF (**green curve**), and GCE/AuNP/NiMOF/AuND (**blue curve**) can be referred to in **Figure 3.7 (A, B)**.

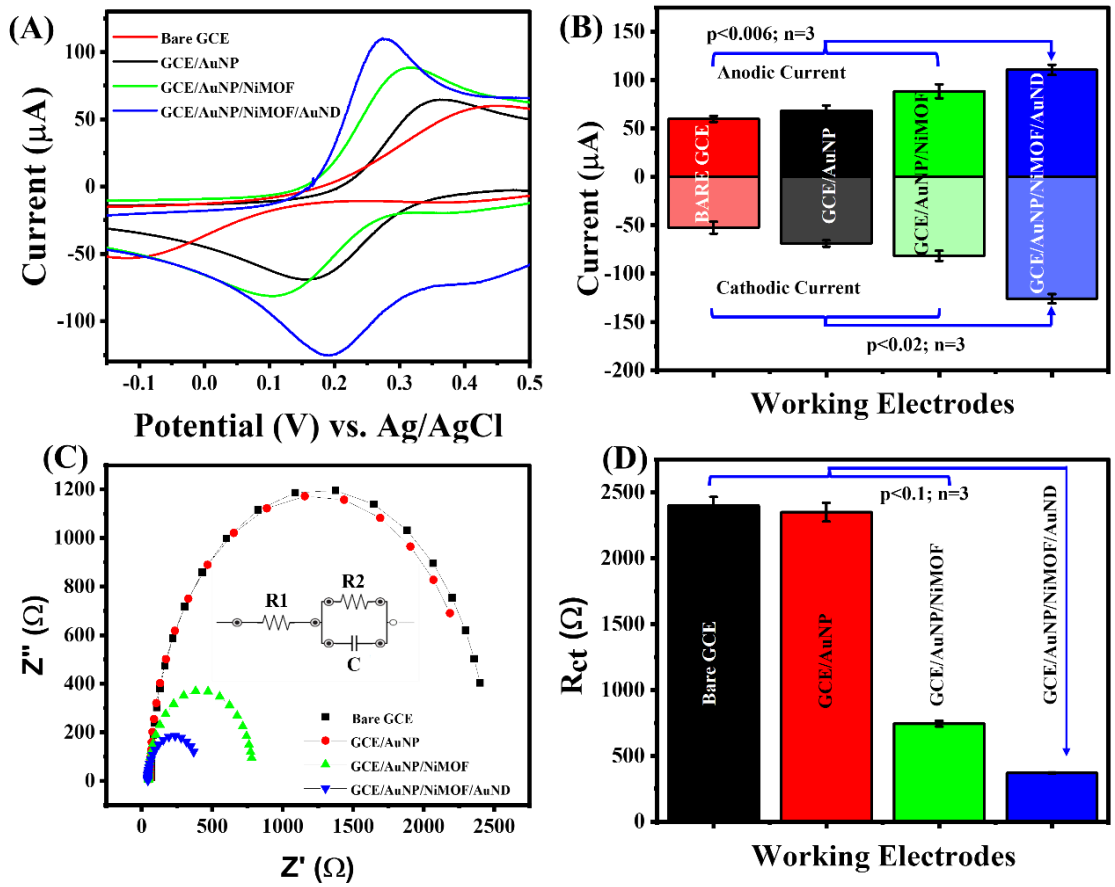

Figure 3.7. ***(A)*** *CV response of bare GCE* ***(red curve)****, GCE/AuNP* ***(black curve)****, GCE/AuNP/NiMOF* ***(green curve),*** *and GCE/AuNP/NiMOF/AuND* ***(blue curve)*** *in ZS (5 mM; pH-7, scan rate- 50 mV/s);* ***(B)*** *A comparative histogram displays the anodic and cathodic current responses corresponding to each surface, with an amplified response for GCE/AuNP/NiMOF/AuND surface.* ***(C)*** *EIS response in the form of Nyquist plots for bare GCE* ***(red curve)****, GCE/AuNP* ***(black curve)****, GCE/AuNP/NiMOF* ***(green curve),*** *and GCE/AuNP/NiMOF/AuND* ***(blue curve)*** *in ZS (5 mM; pH-7) with its equivalent circuit model;* ***(D)*** *A comparative histogram displays the Rct values of each surface, with the least resistance for the final surface.*

MOFs have always been concerning on their usage in sensor matrices due to their compromised conductivity. However, we have been able to cope up with this issue

through the development of conductive NiMOF. The MOF has demonstrated enhanced conductivity when synthesized through the electrochemical route. Apart from this, sandwiching the conductive 2D MOF between the 1D AuNPs and 3D AuNDs through a novel arrangement has resulted in an enhancement in overall surface conductivity considerably (**blue curve**). A comparative histogram has also been added to understand the redox behavior of the electrode with the addition of each layer (**Figure 3.7B**). An enhancement in the current was noted on addition of NiMOF, while the highest peak current was seen in the case of GCE/AuNP/NiMOF/AuND, which was adopted as the final sensing probe. The rise in probe conductivity can be attributed to the metal atom synergies within the sensor matrix. The results were analysed through a t-test, where the p-value was found to be <0.006.

The numerical quantification of individual surface's charge transfer characteristics and deduction of their electrocatalytic activities was done through the estimation of the effective surface area (A) using the Randles-Sevcik's equation as follows,

$$I_p = \left(2.69\times10^5\right) n^{3/2}\, ACD^{1/2}\, v^{1/2} \quad \text{...Equation i}$$

where, Ip is the highest current output (in amperes), n is the no. of electrons involved in redox reaction (here n = 1), A denotes effective surface area of the electrodes (in cm^2), C is the electroactive species' concentration (in mole cm^{-3}), D stands for the diffusion coefficient (in $cm^2\ s^{-1}$) whose value is $7.6 \times 10^{-6}\ cm^2 s^{-1}$ for aqueous ferrocyanide, and v is the scan rate (in Vs^{-1}).

On substituting values in the above equation, the active surface area was found to be 73.2 x 10^{-3} cm^2 for bare GCE, 80.20 x 10^{-3} cm^2 for GCE/AuNP, 108.47 x 10^{-3} cm^2 for GCE/AuNP/NiMOF and 135.55 x 10^{-3} cm^2 for GCE/AuNP/NiMOF/AuND. The results lucidly establish the notion behind addition of subsequent layers and thereby

enhancement of charge transfer ability. The effective surface area in the final sensing probe rises to 1.85 times when compared to bare GCE, 1.69 times when compared to GCE/AuNP and 1.25 times when compared to GCE/AuNP/NiMOF. The validation of these CV outcomes was complimented with the EIS experiments (**Figure 3.7C**). The values obtained by circuit fitting for GCE (**black curve**), GCE/AuNP (**red curve**), GCE/AuNP/NiMOF (**green curve**), GCE/AuNP/NiMOF/AuND (**blue curve**) were plotted in form of their respective Nyquist plots. The corresponding charge transfer resistance (Rct) values were determined for the respective plots as 2401 (±64) Ω for bare GCE, 2350 (±71) Ω for GCE/AuNP, 743.6 (±21.6) Ω for GCE/AuNP/NiMOF and 369.3 (±3.9) Ω for the GCE/AuNP/NiMOF/AuND surface, respectively (**Figure 3.7D**). There was a sharp decline in the Rct on addition of the NiMOF and AuND layers to the surface; thus, the overall EIS findings are in good agreement with the CV results validating the matrix as being conductive.

The charge transfer behaviour and stability of the final probe GCE/AuNP/NiMOF/AuND was elucidated through a scan rate-based study, where the scan rate was varied between 10-100 mV/s in ZS solution. Even at elevated potentials as high as 100 mV/s, the migration of ions on the sensing probe was uninterrupted vouching for the stability of the interface. The square root of scan rates was found to be linearly proportionate to the Ipa and Ipc peak currents, with a correlation coefficient of 0.99, depicting the diffusion-controlled charge transfer behaviour (**Figure 3.8**). The charge transfer capabilities of the GCE/AuNP/NiMOF/AuND matrix paves path for future sensing applications of the developed probe.

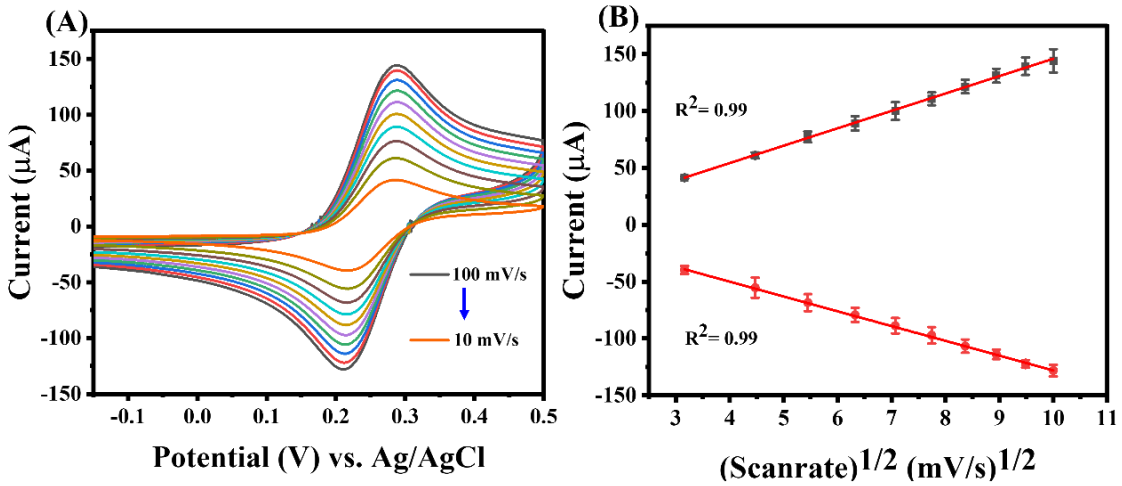

Figure 3.8. ***(A)*** *Scan rate study of the final sandwich sensing probe GCE/AuNP/NiMOF/AuND in ZS when scanned between 100-10 mV/s;* ***(B)*** *Fitting curves corresponding to anodic and cathodic peak currents of the (scan rate)$^{1/2}$ study. The linearity of the plot was deduced with a R^2 value of 0.99 for both fitted curves.*

3.3. Analytical performance of GCE/AuNP/NiMOF/AuND sensor probe

3.3.1. Control studies

A set of control experiments are mandatory to understand the role and stability of the sensing matrix in presence of standard buffers against the target analyte.

Before proceeding towards sensor analytics, a preliminary study must elucidate the contribution of individual layers in the sensing of FA. For this purpose, GCE, GCE/AuNP, GCE/AuNP/NiMOF, and GCE/AuNP/NiMOF/AuND were separately tested against 10^{-7} M FA. A small oxidative current was seen in case of bare GCE, indicating it not being an active electrode for FA sensing. The signal response was also less significant in case of GCE/AuNP which drastically rose in case of GCE/AuNP/NiMOF. The peaks generated in the probe were however slightly shifted towards the negative potential. A distinct and sharper peak with an enormous Ipa at the same potential (i.e., +0.8 V vs. Ag/AgCl), was observed for the GCE/AuNP/NiMOF/AuND sensing probe. Electro-oxidation for FA has been reported at the similar potential in earlier reports on its electrochemical sensing[30]. This could be because of the catalytic response by NiMOF and stable 3D AuND synergy that generated

the optimum signal output **(Figure 3.9A).** The deduced results have been also reported in terms of a simpler histogram comparing their respective Ipa values **(Figure 3.9B).** Therefore, the engineered nanohybrid sandwich model brings out the essence of each component in the detection of FA.

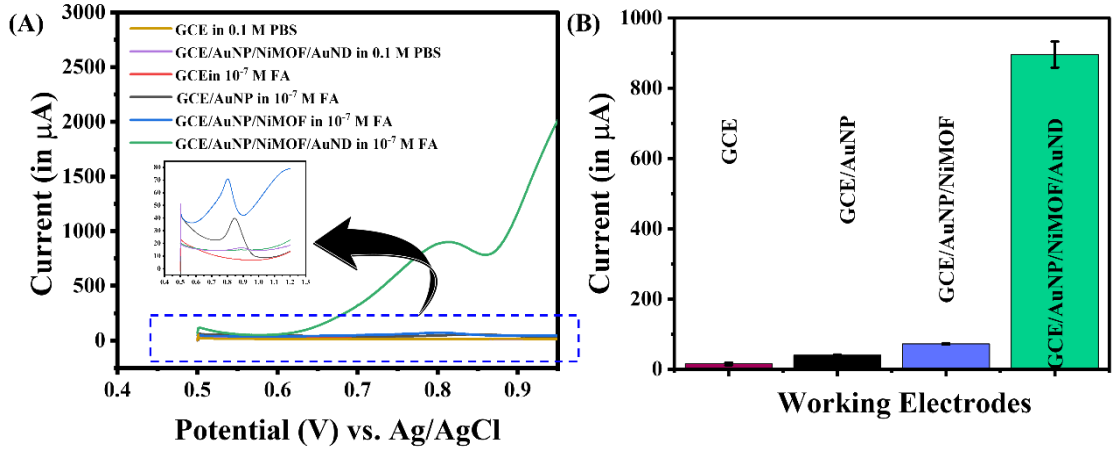

Figure 3.9. ***(A)*** *Layer by layer study against 10^{-7} M concentration of FA* ***(B)*** *Relative histogram for each layer against the tested concentration of FA.*

In order to prove that the signal generated in the first control study was due to FA, we performed the second control experiment. It was important in the perspective to establish the notion that an increase in the current magnitude occurs with an increase in FA concentration due to a precise electron transfer with FA. A voltammetry-based study was conducted considering five concentrations of FA i.e., 10^{-8} M to 10^{-4} M. The current rose gradually with a rise in FA concentration from 10^{-8} M to 10^{-4} M (**Figure 3.10A**). A shift in the peaks on increasing concentration of FA is a common phenomenon, also reported in previous works[20]. The curve exhibited a linear concentration dependent signal output with a correlation coefficient of 0.99 (**Figure 3.10B**). The regression equation obtained from the curve is as follows:

$$\Delta I\ (\mu A) = 4811.037\ (\pm\ 236.46) - 435.19\ (\pm 25.450) \times \log \text{Conc. [FA (M)]}.$$

In a further addition to this, another control test determining the stability of the GCE/AuNP/NiMOF/AuND probe and charge transfer behavior was analysed in the target

analyte. It comprised of a scan rate study between 16 mV/s to 24 mV/s in the presence of 10^{-4} M FA (**Figure 3.10C**). With increase in the scan rate there was observed a linear increment in the Ipa demonstrating an excellent surface stability and diffusion-controlled charge transfer behavior. The anodic current was found to be proportional to the square root of the scan rate with a correlation coefficient of 0.94 (**Figure 3.10D**). Therefore, both the above studies evidently suggested that the designed hybrid sandwich probe is quite stable and efficiently sense FA.

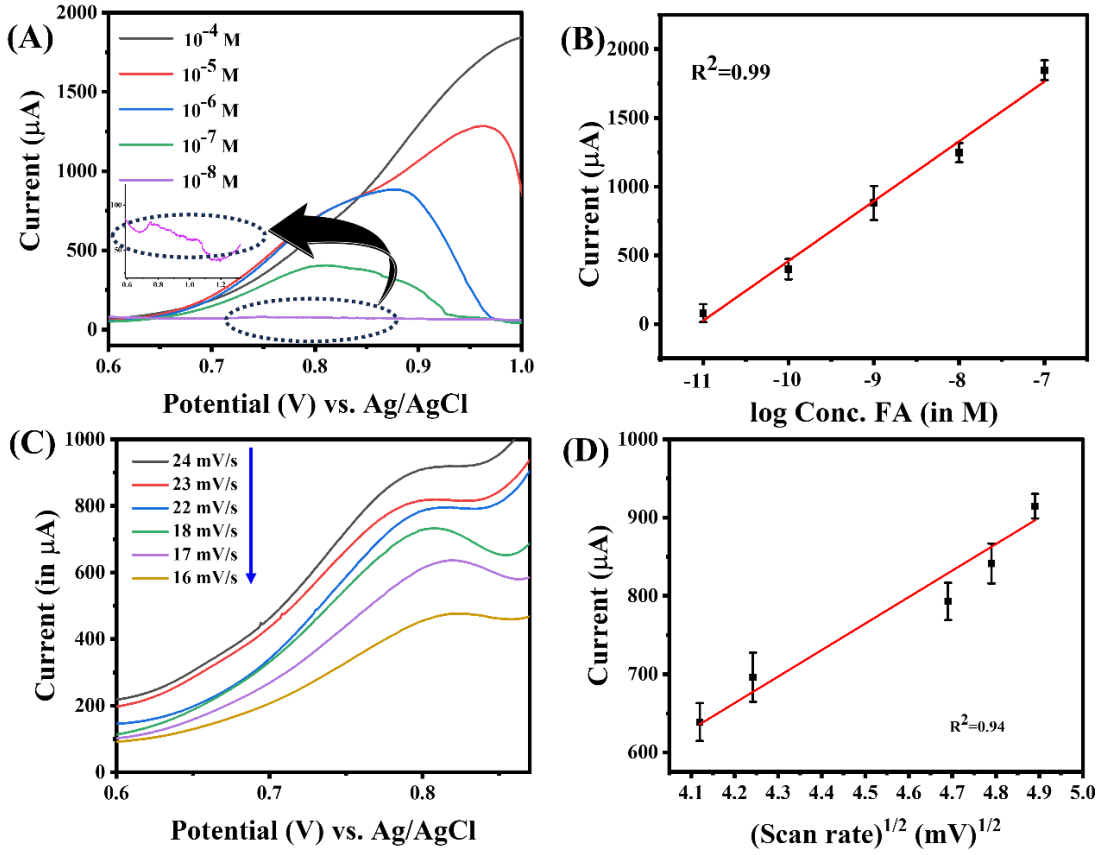

Figure 3.10. ***(A)*** *Concentration dependent study for FA and its corresponding* ***(B)*** *fitting curve, stating a* R^2*=0.99.* ***(C)*** *Scan rate study in the presence of* 10^{-4} *M FA and its corresponding* ***(D)*** *fitting curve for (Scan rate)*$^{1/2}$ *vs. Current (µA).*

There were many reports on the property of FA to adsorb and strongly adhere to sensor surfaces which made us ponder if the same was happening in our case too[30]. Therefore, out of curiosity, we ran a set of experiment where different concentrations of FA treated GCE/AuNP/NiMOF/AuND probe was subjected to FTIR analysis to observe any characteristic peak of FA. To our surprise, the FTIR results were in coherence with our

assumptions. The spectra exhibited characteristic peak of FA in the region (**Figure 3.11, A-D**). The aromatic peaks of FA fall in the region of 1000, 1400 and 1600 cm^{-1} where, the characteristic peak around 1650 cm^{-1} **(region B and C)** corresponds to the -CONH bond while that around 1023 cm^{-1} **(region D)** corresponds to the -NH bond in the FA heterocycles[31]. The broad peaks between 2750-3800 cm^{-1} (**region A**) also signify the presence of -NH and -NH_2 stretching vibrations found in primary and secondary amines of FA [32,33]. The intensity of these peaks proportionately increases with increase in FA concentration (from 10^{-9} M to 10^{-3} M) and is thereby adsorbed on the final sensor.

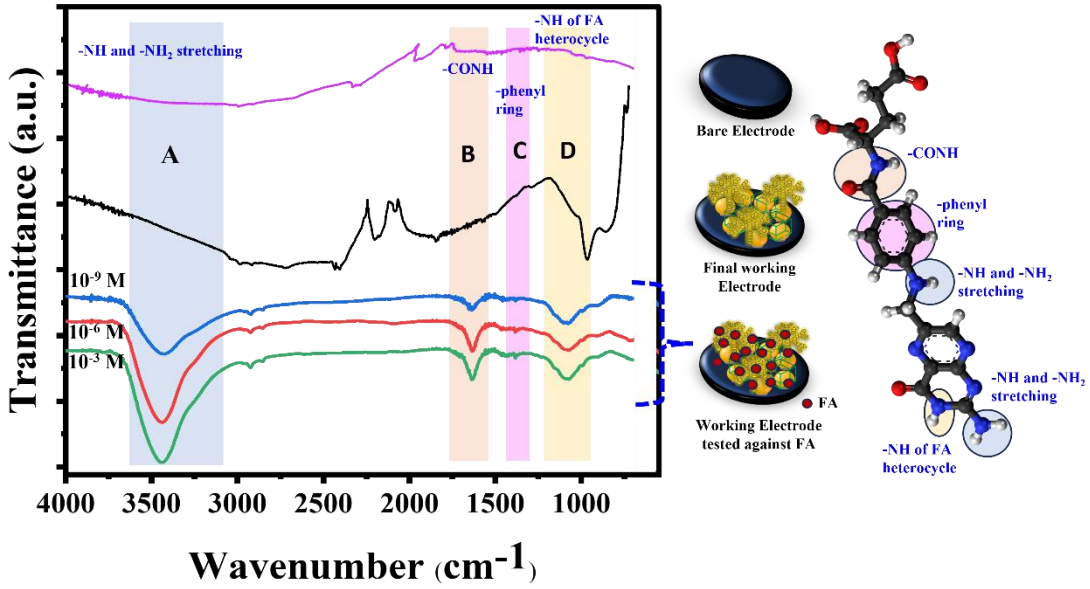

Figure 3.11. *Concentration dependent adsorption study of FA on the GCE/AuNP/NiMOF/AuND probe.*

Also, the wide sensing potential window and broader peaks in FA oxidation are attributed to the strong adsorption behaviour of the phenyl ring of p-aminobenzoic acid moiety of FA[30]. The reason for such adsorption could be most likely the diffusion of FA into the assembly and probably an electrostatic as well as π-π stacking interaction between the aromatic ring of FA and MOF's imidazole in our case. The overall sensing phenomena of FA involves the electro-oxidation of FA at the $C_{(9)}$- $N_{(10)}$ site, where the bicyclic pterin moiety is connected to the p-aminobenzoic acid with the methylene bridge (as depicted in **Figure 3.1**), **panel B**). For a non-enzymatic detection method, tracking the oxidative

cleavage of $C_{(9)}$- $N_{(10)}$ in FA could be a plausible solution. The anodic oxidation of FA yields a single oxidation peak in the potential range of +0.7 V to +1.0 V [30,34] vs. Ag/AgCl in standard buffer solutions due to the conversion of aniline structure in the FA backbone to p-benzoquinone[35]. The further sensing capabilities of the engineered sensor probe was estimated through the method of CA, as discussed in the upcoming section.

3.3.2. Sensor Analytics

CA is a highly sensitive technique which can be a useful tool to understand even a slightest change in the analyte concentration. Hence, the sensing capabilities of the engineered GCE/AuNP/NiMOF/AuND sandwich probe was investigated through it. Initially, the signal output was recorded for the sensor probe in PBS, it being a supporting electrolyte for FA (**blank**). The response was recorded at +0.8 V vs. Ag/AgCl (**blue curve**), followed by evaluation of the probe against varying concentrations of FA. There was a rise in the current magnitude with increasing concentrations of FA from 1 x 10^{-11} M to 1 x 10^{-3} M, with the minimum 'ΔI' between blank and 1 x 10^{-11} M (**Figure 3.12A**). On the basis of the chronoamperometric data, a calibration curve was plotted between the 'ΔI' vs. log [Conc. (FA in M)], refer **Figure 3.12B**. The curve exhibited a linear trend within the evaluated concentration range of FA from 1 x 10^{-11} M to 1 x 10^{-3} with a correlation coefficient of 0.98. The LOD for FA was calculated as 0.48 ± 0.02 x 10^{-11} M using the **equation i** stated below,

$$LOD = \frac{3\mathrm{SD}_b}{Slope} = \frac{3\mathrm{SD}_b}{\frac{dy}{dx}} = \frac{3\mathrm{SD}_b}{\frac{dy}{dlnx}\times\frac{dlnx}{dx}} = \frac{3\mathrm{SD}_b}{\frac{dy}{2.303(dlogx)}\times\frac{1}{x}} = \frac{3\times2.303\times\mathrm{SD}_b\times x}{\frac{dy}{dlogx}} = \frac{3\times2.303\times\mathrm{SD}_b\times x}{Slope\ of\ semilog\ plot} \quad \textit{…Equation i}$$

where SD_b represents the SD of the blank, and x is the lowest concentration measured.

The linear increment in amperometry current responses with rise in FA concentrations from 1 x 10^{-11} M to 1 x 10^{-3} M can be represented through the regression equation as,

$$I\ (\mu A) = 0.865\ (\pm 0.035) + 0.072\ (\pm 0.0042)\ \log \text{Conc. [FA (M)]}.$$

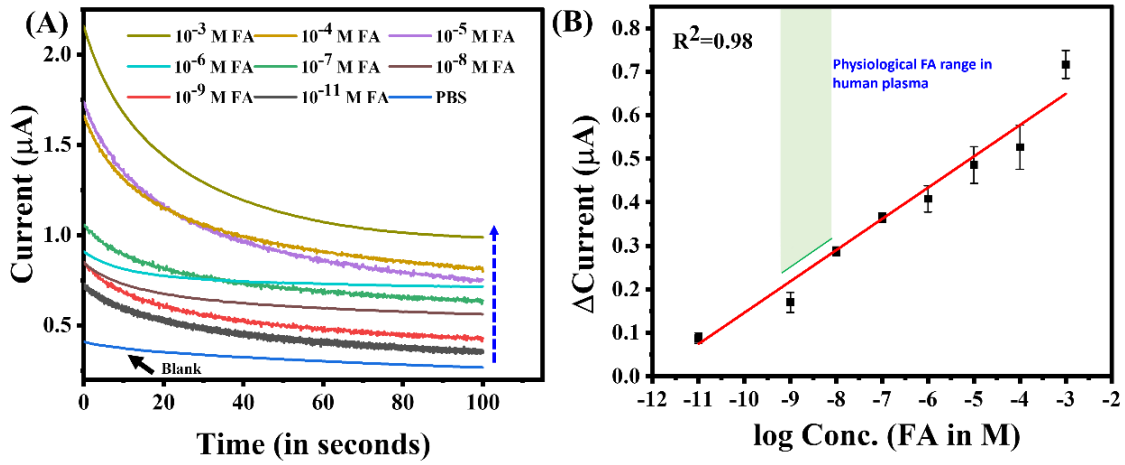

Figure 3.12. ***(A)*** *Chronoamperometric response curve of the final sensing probe against varying concentrations of FA, ranging from 1 x 10^{-3} M to 1x 10^{-11} M.* ***(B)*** *Calibration plot for the same range of FA with an R^2 of 0.98.*

3.3.3. Response time study

Response time refers to the time lapsed for a sensor to respond towards a change in the concentration of buffer on addition of a known concentration of analyte into it. The shorter the response time of a sensor, the more it is believed to be sensitive towards the target analyte [36]. For examining the same for our engineered GCE/AuNP/NiMOF/AuND surface, CA was used as the suitable method, where at +0.8 V vs. Ag/AgCl, different concentrations of FA were injected in blank PBS solution to evaluate the response of the sensor. **Figure 3.13** shows a typical chronoamperometric response of the sensor towards injection of 200 µl of 10^{-8} M FA. In the curve, the sample is injected to stable current **(a)** at a given point of time **(b),** where a sharp rise in current is noted due to diffusion which goes up to **(c)** within a time span of 1232.01 seconds and 1233.94 seconds. Then, the current gradually decreases with time to reach a plateau, termed as 'current saturation' at **(d)**. The saturation current (d) and injection point current (b) possesses a significant

difference (ΔI) by virtue of the added FA to PBS electrolytic solution that oxidises contributing electrons. For FA concentration as low as 10^{-8} M, the sensor responded within 1.93 seconds. We had recorded responses for different concentrations and the time lapsed was low for higher concentrations and vice-versa. A table showing response time pertaining to different concentrations of FA viz. 10^{-4} M, 10^{-6} M, 10^{-9} M, has been mentioned in **Table 3.1.** A slight change in the response time was noted with change in concentrations, however remained constrained to **<2.1** seconds, indicating the rapid sensing ability of the system. The fast response of the probe is by virtue of three diversified layers, that are individually contributing towards analyte sensing.

Table 3.1. *Response time values for different concentrations of FA.*

Concentration of FA	***Response Time***
10^{-4} M	*1.42 sec*
10^{-6} M	*1.62 sec*
10^{-8} M	*1.93 sec.*
10^{-9} M	*1.9 sec.*
10^{-9} M	*2 sec.*
Average Response Time	<2.1 seconds

The engineered 3D sensing probe is an interesting surface because of its short and simple fabrication strategy without the involvement of hefty chemical synthesis-based processes, a wide LDR and low LOD against FA with a lightning-fast response time. A relative evaluation of the developed probe and its parameters with other recently reported FA sensor probe has been summarized in **Table 3.2**.

It is interesting to note that where most of the reported MOF-based FA detection systems have a LOD in the mM ranges, our developed sensor has almost 7 orders lower LOD than the recently reported setups with much simpler fabrication steps and better response time, intersecting the clinical ranges.

Table 3.2. *Comparative analysis of recently developed FA sensors comprising MOF as transduction system component with our developed system.*

Probe Composite	Fabrication strategy	Technique used	Probe/matrix fabrication time	Reaction time	LOD	LDR	Real Sample	Reference
RE-MOF (Rare earth MOFs, where RE= Eu, Gd, Tb and Dy	A series of water stable 3D RE-MOFs were synthesized solvothermally in a mixture of DMF and water solvent to yield the fluorescent MOFs.	Fluorescence	Nearly 120 hours	N.R.	0.02 mM	0-120 µM	N.R.	[37]
Ni-MOF	Ni-BTC MOF was synthesized through the solvothermal route. A 1 mg/ml solution of the MOF in deionized water was ultrasonicated and dropcasted onto a unmodified SPE surface to form the WE.	CA, DPV	36 hours	N.R.	0.03±0.001 µM	0.08 to 635.0µM	FA tablets, urine	[38]
La^{+3}/Co_3O_4 nano-cubes	Carbon SPE working electrodes were coated with an aliquot of La^{+3}/Co_3O_4 nano-cubes dispersed in aqueous system. The modified electrode was allowed to dry at RT before use in sensing.	CA, DPV	>16 hours	N.R.	0.3 µM	1.0-600.0 µM	FA tablets, urine	[39]
Zn-Eu MOF	A heterometallic MOF was prepared through the solvothermal route. It was suctioned with filter paper to obtain MOF-based test strips of the size 1 cm x 2 cm.	Fluorescence	>147 hours	N.R.	1.84×10^{-8} M	5.90×10^{-4} to 2.22×10^{-7} M	N.R.	[40]
ZIF-90	7-amino-4-methylcoumarin was encapsulated within ZIF-90 to fabricate a fluorescent sensor at RT.	Fluorescence	>9 hours	N.R.	3.5 x 10-6 M	1×10^{-5} to 1×10^{-3} M	Milk, Goat serum	[41]
Eu/Tb/Gd MOF (Ln MOF)	Three isostructural MOFs were synthesized solvothermally at 160 °C which was thereafter used for optical sensing of FA.	Fluorescence	>72 hours	1.5 minutes	0.0883µM	0–18 µM	N.R.	[24]
Ag MOF	The Ag-based MOF was synthesized through the solvothermal route at 160 °C to obtain needle-like crystals.	Fluorescence	>84 hours	5 min.	49 nM	0.1–30 µM	Human serum and plasma	[42]
ZIF-67/AgNWs	Screen printed carbon electrodes were modified through dropping them with a layer of ZIF-67/AgNWs and airdried at RT to form the final working sensor probe.	SWV	>24 hours	N.R.	30 nM.	0.1 µM to 10 µM	Real serum samples	[35]
MB/ERGO/ GCE	On a polished GCE surface, GO was deposited electrochemically forming ERGO/GCE which was then modified by	DPV	>25 hours for GO preparation followed by EC based depositions	N.R.	0.5 mM	4.0 mM to 167 mM	Commercial FA tablets	[20]

	further deposition of MB on its surface through CV.							
CuONPs/poly MO	A clean and polished GCE surface was drop-coated with a film of CuONPs dispersed in EtOH. This was followed by modification of the surface using MO poly-electrodeposition onto the GCE using CV.	DPV, CA	> 3 hours	N.R.	0.002 μM	0.01 to 1.5 μM	Fresh citrus juices (orange, tomato, and strawberry	[43]
NC/CPE (Niacin-modified carbon paste electrode)	Initially, CPE was fabricated from scratch using ground GO and binder. A niacin monomeric solution was electrodeposited onto the CPE through 15 cycles of CV.	CV	N.R.	N.R.	0.09 μM	5.0 μM to 45.0 μM	Fruit juice (orange, lemon and tomato, pharmaceutical sample	[44]
C/PDA/AuNPs	PDA encapsulated carbon-based material adorned with AuNPs was synthesized through a microwave-assisted approach to be used as a WE.	CA	N.R.	5 minutes	25 nM	0.1–905 _ μM	Human serum	[45]
PtNPs-GNPs-MWCNTs-β-CD	Initially, a homogeneous dispersed solution of GNPs, MWCNTs and PtNPs was prepared in water followed by addition of β-CD to it and thereby sonication. The reaction yielded PtNPs-GNPs-MWCNT-β-CD composite which was drop-coated on a polished GCE surface to form the WE.	CV	>10 minutes	N.R.	0.48 μmol L^{-1}	0.02–0.50 mmol L^{-1}	FA tablets	[46]
AuNP/NiMOF/AuND	**A layer of conductive NiMOF was sandwiched between layers of AuNPs and AuNDs.**	**DPV, CA**	**<40 minutes**	**1.5 seconds**		**10^{-3} – 10^{-11} M**	**Serum and MCF-7 cells**	***This work***

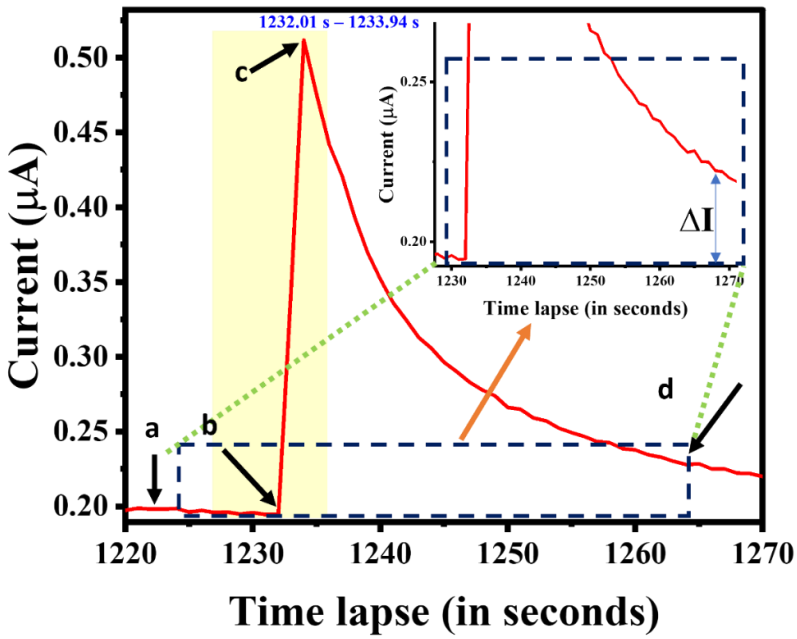

Figure 3.13. *The graph denotes the response time curve of the developed sensor probe against spiking 10^{-8} M FA concentration in standard buffer, where* ***(a)*** *is stable current* ***(b)*** *injection point* ***(c)*** *maximum current spike on FA inoculation, and* ***(d)*** *saturation current. (inset) shows the current plateau observed on the recovery stage post FA injection, denoted by ΔI.*

3.3.4. Selectivity and reproducibility assay

The translational significance of the developed GCE/AuNP/NiMOF/AuND sandwich probe can only be proven if its specificity is towards the target analyte at a given potential when tested against co-existing interferent species. Therefore, a variety of interferent molecules (e.g., L-histidine, sucrose, ß-alanine, urea, glucose, caffeine) were chosen along with our target analyte FA to be tested against the sensor probe in the similar experimental conditions. **Figure 3.14A** demonstrates a comparative histogram of the sensor selectivity against a range of interferents with comparison to our target analyte. An equation (**Equation ii)** to determine the coefficient of selectivity (K_{sel}) was used for the co-existing molecules. The obtained values have been tabulated in **Table 3.3**. The values were found to be significantly low ($K_{sel.}$ <<1), with p-value <0.0001 emphasizing an extremely fair selectivity of the developed GCE/AuNP/NiMOF/AuND probe for FA.

$$K_{sel} = Signal_{interfering\ molecule}/Signal_{FA} \qquad \textbf{...Equation ii}$$

where $K_{sel.}$ stands for the coefficient of selectivity, $(Signal)_{interfering\ molecules}$ is the current response of the probe corresponding to specific interferant, and $(Signal)_{FA}$ is the response obtained from probe after being tested for FA.

The passivity of the developed GCE/AuNP/NiMOF/AuND sensor probe resulted to no considerate signal output generation against only the interferants molecules at the specific potential.

Table 3.3. *Table discussing $K_{sel.}$ of the sensor against a range of analytes.*

Co-existing molecules	Current (µA)	$K_{sel.}$
PBS	0.047	0.059
L-histidine	0.051	0.065
sucrose	0.080	0.102
beta alanine	0.099	0.126
Urea	0.057	0.072
Glucose	0.093	0.118
caffeine	0.094	0.120
Folic acid	0.783	1

Five different electrodes were fabricated with the same methodology and tested discretely against the same concentration (10^{-3} M) of FA to verify the electrode-to-electrode reproducibility where negligible variations were observed (**RSD <3.5**). The stability of the surface was due to direct electrodeposition of the structural architecture and no involvement of any biorecognition elements (antibodies, enzymes, aptamers, etc.) during its fabrication imparted the GCE/AuNP/NiMOF/AuND sensing probe with good stability (**Figure 3.14B)**.

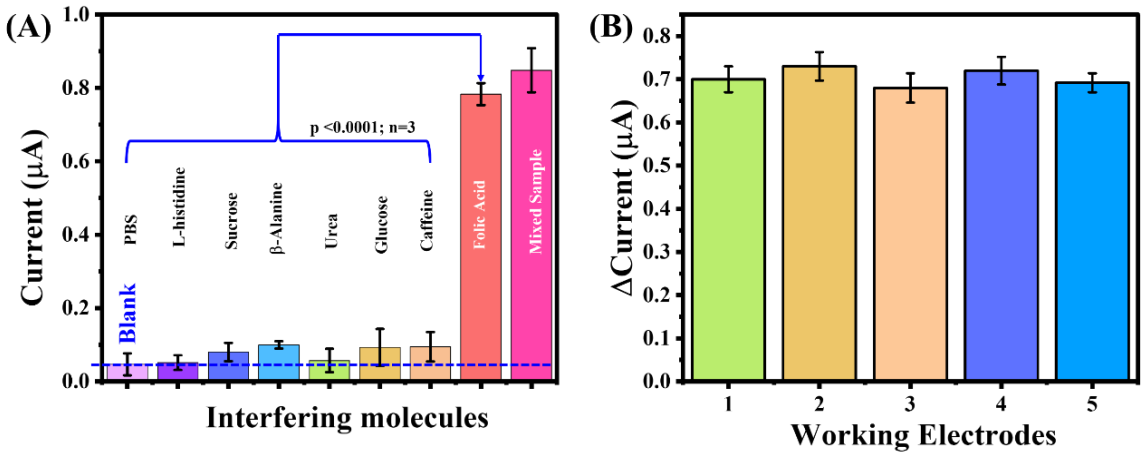

Figure 3.14. ***(A)*** *Interference study for the developed sensing probe against a range of competitive possible interferents,* ***(B)*** *The probe reproducibility was checked across a range of different electrodes fabricated under similar circumstances***.**

Further FA was measured using the GCE/AuNP/NiMOF/AuND probe in serum samples and *in vitro* microenvironment in order to evaluate the practicability of our developed sensing matrix as discussed in the upcoming section.

3.3.5. Real sample analysis

3.3.5.1. Serum-sample based study

FA is an important biomolecule in regulating cellular pathways, and diverse metabolic roles[42]. Hence, its quantitative analysis in serum poses enormous clinical significance. The serum-based study was conducted by testing the developed sensing probe against different concentrations of FA-spiked serum samples. The spike and test recovery model were used to evaluate the sensor performance. Initially, the procured serum sample was equilibrated in PBS, following which it was further spiked with different known concentrations of FA and current response was documented. The experiments were conducted in triplicates under optimized experimental settings.

The FA recovery percentage was calculated using equation, as stated below,

$$\%\, Recovery = (S_{FA} - B_{FA})/(SS_{FA}) * 100 \qquad \text{....}\textbf{\textit{Equation iii}}$$

where, $[S]_{FA}$ and $[B]_{FA}$ correspond to the analytical response of GCE/AuNP/NiMOF/AuND nanohybrid sensing probe carried out in serum samples spiked with FA and blank sample, respectively; $[SS]_{FA}$ refer to the response generated in standard buffer (PBS in this case) with same concentration of FA.

The current response pertaining to different concentrations of FA in serum has been represented through a calibration curve reported in **Figure 4B (red curve)** and compared with the standard calibration curve for FA in PBS. There was an incremental shift in the current magnitude with increasing concentration of the target analyte, with the current recovery ranging between 95.11-98.17%. The mathematical representation of signal outcome can be denoted by the equation, $\Delta I\ (\mu A) = 0.850\ (\pm 0.038) + 0.071\ (\pm 0.005) \log$ Conc. [FA (M)]. The sensor efficiency was found commendable even in serum samples with a correlation coefficient of 0.96. The comparable results with the standard calibration plot vouch for sensor efficiency however, slight deviations in current magnitude could be an impact of handling or minor ion mobility changes in matrix. The different serum constituents however did not impact much on the experimental data therefore, making it a suitable sensing probe for precise FA monitoring, evoking its future commercial aspects.

Further, *in vitro* studies were attempted for the sensing probe to re-affirm its utility in real cellular microenvironment.

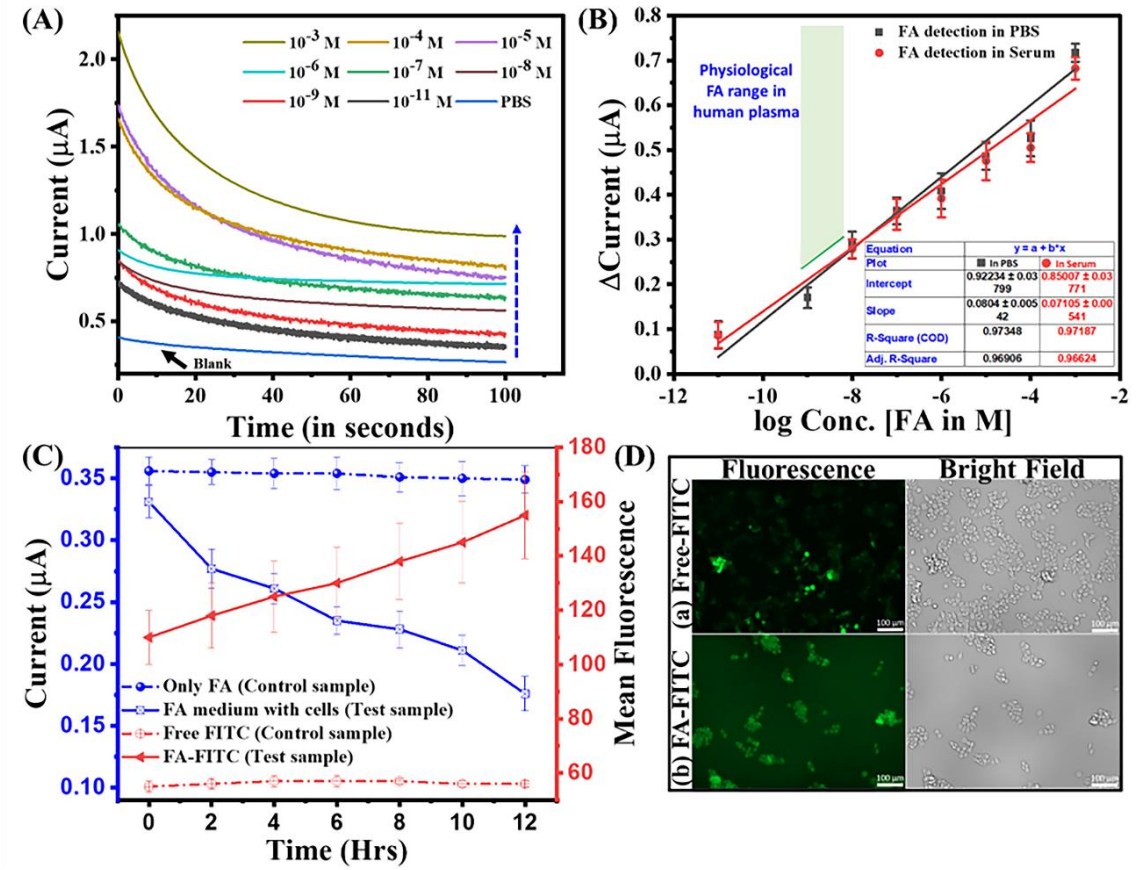

Figure 3.15. ***(A)*** *Chronoamperometric response curve of the final sensing probe against varying concentrations of FA, ranging from 1x 10^{-11} M to 1 x 10^{-3} M;* ***(B)*** *Calibration curves for FA detection in standard PBS buffer and serum sample with an R^2 value of 0.969 and 0.966, respectively;* ***(C)*** *A comparative FA uptake analysis in in vitro cellular microenvironment by developed sensor (blue curves) and its validation through standard fluorescence technique (red curves). Fluorescence intensity and current output was mapped over time for both control and test samples;* ***(D)*** *Fluorescence (left panel) and bright field images (right panel) comparing the uptake of free FITC (control sample) and FA-FITC conjugates (test sample) by MCF-7 cells:* ***(a)*** *Cells incubated with free FITC show minimal and non-specific fluorescence,* ***(b)*** *Cells incubated with FA-FITC conjugates display enhanced and widespread fluorescence, suggesting active and specific uptake of the conjugate. Bright field images confirm the presence of cells in both conditions (images represented at 100 μm scale).*

3.3.5.2. In vitro sensing using MCF-7 cell lines and its validation through fluorescence imaging

Certain types of cancer cells are known for their folic acid receptor (FAR) overexpression characteristics, one being MCF-7 cells as well[47]. In our study, we attempted to recreate the cancer cellular uptake microenvironment for FA, where MCF-7 cell lines were grown in controlled systems and the media concentration of FA was recorded (**Figure 3.15C**). The rationale behind using cancer cells as the test system instead of a normal cell system

is to govern FA cellular uptake in a shorter time frame, taking aid of its FAR overexpression. MCF-7 cells of the same cellular confluency growing in different wells of a well plate was inoculated with the same concentration (10^{-4} M) of FA. It is important to note that the cells were cultured in a FA-free media to avoid any false positive results. A time dependent study was conducted, where the cells uptake FA naturally and its concentration in media decreases over time which was determined over a span of 0 hours to 12 hours through the developed sensor. We also performed a negative control experiment, where free FA was injected in a cell free media. Fresh test samples (i.e., 1 ml FA inoculated media in cellular microenvironment) were procured at every 3 hours and tested for the presence of FA. With subsequent readings, a decline in FA concentration within cellular microenvironment was noted affirming the successful FA uptake by growing MCF-7 cells as depicted in **blue solid curve** of **Figure 3.15C**. No change in current response was noted for the control test samples **(blue dotted curve)** as there was no cells to uptake FA. To validate the results through a standard method, a time dependent FA uptake study was conducted in the MCF-7 cells through detailed fluorescence-based analysis via live cell imaging[48]. **Figure 3.15C** depicts fluorescence and bright field images demonstrating MCF-7 cells' uptake of FA-FITC conjugates (test sample) and free FITC (control sample). In this, FA-FITC conjugate uptake was monitored in MCF-7 cells as a function of time from 0 to 12 hours through continuous live cell imaging. There was a constant increase in fluorescence intensity over time in FA-FITC sample, starting from around 112 at 0 hours and increasing to around 155 at 12 hours **(red solid curve)**. This increase shows active uptake of the FA-FITC conjugate by MCF-7 cells. In contrast, the fluorescence intensity of the control group (free FITC) remains relatively low and consistent over the same period **(red dotted curve),** demonstrating minimal or no uptake in the absence of folic acid conjugation. The results were recorded at multiple zones and

in triplicate. The mapped data results of the live cell imaging and sensor makes the discussion more lucid, where the graphs are inversely directing the whole phenomena. With a decline in the media/extracellular FA concentrations, there is an enhancement in the fluorescent intensity corresponding to increased FA-FITC conjugate uptake within the cells with each passing hour. Thus, the study re-confirmed three important inferences as follows: (i) the MCF-7 cells actively uptake spiked FA from cellular microenvironment; (ii) the sensor is capable of detecting cellular FA uptake over a period of time with even in the slightest change of concentrations; (iii) the system is highly stable in such complex cellular microenvironment with highly precise estimation of FA in extracellular premises.

4. Conclusion

The work focusses on the development of a novel sandwich sensing probe for monitoring a physiologically significant vitamin (FA) through electrochemical route. The sandwich probe was fabricated by optimization of process parameters to replace existing tedious MOF synthesis process by a simpler electrochemical approach, followed by its conjugation with Au nanostructures. It was further characterized through AFM, SEM, EDX and electrochemical methods to deploy against detection of the target analyte in serum and cellular microenvironment. The inter-junction of Au based surfaces with a highly catalytic Ni-centered MOF resulted into a hybrid catalytic surface with superior charge transfer characteristics and analytical performance. The calibration study yielded a linear slope within a FA concentration range of 1×10^{-11} and 1×10^{-3} M and a LOD of $0.48 \pm 0.02 \times 10^{-11}$ M. A wide LDR is of great significance since dietary supplements can raise the blood FA concentration in µM. Thus, the developed sensor is capable of detecting FA in both cases i.e. FA deficiency or FA accumulation. The engineered sensor probe displayed a commendable response time of less than 2.1 seconds, attributing to its

excellent sensitivity towards FA determination. When subjected to significantly higher concentrations of interfering species prevalent in the biological microenvironment, it could easily selectively detect FA with $K_{sel} << 1$. The results were also quite promising in real sample matrices wherein the outcomes were in consistency with the standard conditions. The proposed sensor displays good current recovery percentages and therefore, could be an optimal promising platform for sensitive detection of FA in serum as well as other biological samples. To our knowledge, the devised sandwich model sensor is one of its kind incorporating easy fabrication steps, remarkable charge transfer characteristics and a wide detection range for analytes like FA covering its clinical range and beyond. The developed system can be further deployed for future integrations within multiplexing setups for a simultaneous and rapid detection of diverse analytes.

REFERENCES

(1) Lavanya, N.; Fazio, E.; Neri, F.; Bonavita, A.; Leonardi, S. G.; Neri, G.; Sekar, C. Electrochemical Sensor for Simultaneous Determination of Ascorbic Acid, Uric Acid and Folic Acid Based on Mn-SnO2 Nanoparticles Modified Glassy Carbon Electrode. *J. Electroanal. Chem.* **2016**, *770*, 23–32. https://doi.org/10.1016/j.jelechem.2016.03.017.

(2) Di Tinno, A.; Cancelliere, R.; Micheli, L. Determination of Folic Acid Using Biosensors—a Short Review of Recent Progress. *Sensors* **2021**, *21* (10). https://doi.org/10.3390/s21103360.

(3) Langston, B. Y. W. C.; Darby, W. J.; Shukers, C. F.; Day, P. L.; Ph, D. N U T R I T I O N A L CYTOPENIA (VITAMIN M D E F I C I E N C Y) (From the School of Medicin ,, University of Arkansas , Little Rock). **1938**.

(4) Andlid, T. A.; D'Aimmo, M. R.; Jastrebova, J. Folate and Bifidobacteria. *Bifidobact. Relat. Org. Biol. Taxon. Appl.* **2018**, No. October, 195–212. https://doi.org/10.1016/B978-0-12-805060-6.00011-9.

(5) Baghbamidi, S. E.; Beitollahi, H.; Mohammadi, S. Z.; Tajik, S.; Soltani-Nejad, S.; Soltani-Nejad, V. Nanostructure-Based Electrochemical Sensor for the Voltammetric Determination of Benserazide, Uric Acid, and Folic Acid. *Cuihua Xuebao/Chinese J. Catal.* **2013**, *34* (10), 1869–1875. https://doi.org/10.1016/s1872-2067(12)60655-x.

(6) Mazloum-Ardakani, M., Beitollahi, H., Mirjalili, B. B. F., & Akbari, A. Determination of Epinephrine in the Presence of Uric Acid and Folic Acid Using Nanostructure-Based Electrochemical Sensor. *J. Nanostructures* **2012**, *1*, 181–190.

(7) Mazloum-Ardakani, M.; Hosseinzadeh, L.; Khoshroo, A.; Naeimi, H.; Moradian, M. Simultaneous Determination of Isoproterenol, Acetaminophen and Folic Acid Using a Novel Nanostructure-Based Electrochemical Sensor. *Electroanalysis* **2014**, *26* (2), 275–284. https://doi.org/10.1002/elan.201300401.

(8) Kanchana, P.; Sekar, C. Development of Electrochemical Folic Acid Sensor Based on Hydroxyapatite Nanoparticles. *Spectrochim. Acta - Part A Mol. Biomol. Spectrosc.* **2015**, *137*, 58–65. https://doi.org/10.1016/j.saa.2014.07.087.

(9) Vollset, S. E.; Clarke, R.; Lewington, S.; Ebbing, M.; Halsey, J.; Lonn, E.; Armitage, J.; Manson, J. E.; Hankey, G. J.; Spence, J. D.; Galan, P.; Bønaa, K. H.; Jamison, R.; Gaziano, J. M.; Guarino, P.; Baron, J. A.; Logan, R. F. A.; Giovannucci, E. L.; Den Heijer, M.; Ueland, P. M.; Bennett, D.; Collins, R.; Peto, R. Effects of Folic Acid Supplementation on Overall and Site-Specific Cancer Incidence during the Randomised Trials: Meta-Analyses of Data on 50 000 Individuals. *Lancet* **2013**, *381* (9871), 1029–1036. https://doi.org/10.1016/S0140-6736(12)62001-7.

(10) Figueiredo, J. C.; Grau, M. V; Haile, R. W.; Sandler, R. S.; Summers, R. W.; Bresalier, R. S.; Burke, C. A.; McKeown-Eyssen, G. E.; Baron, J. A. Folic Acid and Risk of Prostate Cancer: Results From a Randomized Clinical Trial. *JNCI J. Natl. Cancer Inst.* **2009**, *101* (6), 432–435. https://doi.org/10.1093/jnci/djp019.

(11) Cole, B. F.; Baron, J. A.; Sandler, R. S.; Haile, R. W.; Ahnen, D. J.; Bresalier, R. S.; McKeown-Eyssen, G.; Summers, R. W.; Rothstein, R. I.; Burke, C. A.; Snover, D. C.; Church, T. R.; Allen, J. I.; Robertson, D. J.; Beck, G. J.; Bond, J. H.; Byers, T.; Mandel, J. S.; Mott, L. A.; Pearson, L. H.; Barry, E. L.; Rees, J. R.; Marcon, N.; Saibil, F.; Ueland, P. M.; Greenberg, E. R.; Polyp Prevention Study Group, for the. Folic Acid for the Prevention of Colorectal AdenomasA Randomized Clinical Trial. *JAMA* **2007**, *297* (21), 2351–2359. https://doi.org/10.1001/jama.297.21.2351.

(12) Yang, Q.; Cogswell, M. E.; Hamner, H. C.; Carriquiry, A.; Bailey, L. B.; Pfeiffer, C. M.; Berry, R. J. Folic Acid Source, Usual Intake, and Folate and Vitamin B-12 Status in US Adults: National Health and Nutrition Examination Survey (NHANES) 2003–20061234. *Am. J. Clin. Nutr.* **2010**, *91* (1), 64–72. https://doi.org/https://doi.org/10.3945/ajcn.2009.28401.

(13) Matias, R.; Ribeiro, P. R. S.; Sarraguça, M. C.; Lopes, J. A. A UV Spectrophotometric Method for the Determination of Folic Acid in Pharmaceutical Tablets and Dissolution Tests. *Anal. Methods* **2014**, *6* (9), 3065–3071. https://doi.org/10.1039/c3ay41874j.

(14) Kanjilal, G.; Mahajan, S. N.; Rao, G. R. Colorimetric Determination of Folic Acid in Pharmaceutical Preparations. *Analyst* **1975**, *100* (1186), 19–24. https://doi.org/10.1039/AN9750000019.

(15) Bertuzzi, T.; Rastelli, S.; Mulazzi, A.; Rossi, F. LC-MS/MS Determination of Mono-Glutamate Folates and Folic Acid in Beer. *Food Anal. Methods* **2019**, *12* (3), 722–728. https://doi.org/10.1007/s12161-018-1396-6.

(16) Rodríguez Flores, J.; Peñalvo, G. C.; Mansilla, A. E.; Gómez, M. J. R. Capillary Electrophoretic Determination of Methotrexate, Leucovorin and Folic Acid in Human Urine. *J. Chromatogr. B* **2005**, *819* (1), 141–147. https://doi.org/https://doi.org/10.1016/j.jchromb.2005.01.039.

(17) Osseyi, E. S.; Wehling, R. L.; Albrecht, J. A. HPLC Determination of Stability and Distribution of Added Folic Acid and Some Endogenous Folates During Breadmaking. *Cereal Chem.* **2001**, *78* (4), 375–378. https://doi.org/https://doi.org/10.1094/CCHEM.2001.78.4.375.

(18) Song, Z.; Wang, L. Chemiluminescence Inhibition Assay for Folic Acid Using Flow Injection Analysis. *Phytochem. Anal.* **2003**, *14* (4), 216–220. https://doi.org/https://doi.org/10.1002/pca.704.

(19) Hoegger, D.; Morier, P.; Vollet, C.; Heini, D.; Reymond, F.; Rossier, J. S. Disposable Microfluidic ELISA for the Rapid Determination of Folic Acid

Content in Food Products. *Anal. Bioanal. Chem.* **2007**, *387* (1), 267–275. https://doi.org/10.1007/s00216-006-0948-6.

(20) Zhang, D.; Ouyang, X.; Ma, W.; Li, L.; Zhang, Y. Voltammetric Determination of Folic Acid Using Adsorption of Methylene Blue onto Electrodeposited of Reduced Graphene Oxide Film Modified Glassy Carbon Electrode. *Electroanalysis* **2016**, *28* (2), 312–319. https://doi.org/10.1002/elan.201500348.

(21) Chung, S.; Chandra, P.; Koo, J. P.; Shim, Y.-B. Development of a Bifunctional Nanobiosensor for Screening and Detection of Chemokine Ligand in Colorectal Cancer Cell Line. *Biosens. Bioelectron.* **2018**, *100*, 396–403. https://doi.org/https://doi.org/10.1016/j.bios.2017.09.031.

(22) Shubhangi; Nandi, I.; Rai, S. K.; Chandra, P. MOF-Based Nanocomposites as Transduction Matrices for Optical and Electrochemical Sensing. *Talanta* **2024**, *266* (P2), 125124. https://doi.org/10.1016/j.talanta.2023.125124.

(23) Shubhangi, N.; Kumari, R.; Rai, S. K.; Chandra, P. Electrochemical Assembly of Nickel Metal Organic Framework-Decorated Nanoimprinted Gold Dendrites as Peroxidase Mimic for High-Performance Hydrogen Peroxide Sensing. *ACS Appl. Nano Mater.* **2024**, *7* (1), 1388–1401. https://doi.org/10.1021/acsanm.3c05396.

(24) Dong, Z.-P.; Zhao, F.; Zhang, L.; Liu, Z.-L.; Wang, Y.-Q. A White-Light-Emitting Lanthanide Metal–Organic Framework for Luminescence Turn-off Sensing of MnO4− and Turn-on Sensing of Folic Acid and Construction of a "Turn-on plus" System. *New J. Chem.* **2020**, *44* (25), 10239–10249. https://doi.org/10.1039/D0NJ02145H.

(25) Kumari, R.; Dkhar, D. S.; Mahapatra, S.; Divya; Singh, S. P.; Chandra, P. Nano-Engineered Surface Comprising Metallic Dendrites for Biomolecular Analysis in Clinical Perspective. *Biosensors* **2022**, *12* (12). https://doi.org/10.3390/bios12121062.

(26) Kumari, R.; Chandra, P. Electrochemical Nano-Imprinting of Trimetallic Dendritic Surface for Ultrasensitive Detection of Cephalexin in Pharmaceutical Formulations. *Pharmaceutics* **2023**, *15* (3). https://doi.org/10.3390/pharmaceutics15030876.

(27) Mahato, K.; Nagpal, S.; Shah, M. A.; Srivastava, A.; Maurya, P. K.; Roy, S.; Jaiswal, A.; Singh, R.; Chandra, P. Gold Nanoparticle Surface Engineering Strategies and Their Applications in Biomedicine and Diagnostics. *3 Biotech* **2019**, *9* (2), 57. https://doi.org/10.1007/s13205-019-1577-z.

(28) M. V., V.; Nageswaran, G. Review—Direct Electrochemical Synthesis of Metal Organic Frameworks. *J. Electrochem. Soc.* **2020**, *167* (15), 155527. https://doi.org/10.1149/1945-7111/abc6c6.

(29) Shooshtari Gugtapeh, H.; Rezaei, M. One-Step Electrodeposition of a Mesoporous Ni/Co-Imidazole-Based Bimetal-Organic Framework on Pyramid-like NiSb with Abundant Coupling Interfaces as an Ultra-Stable Heterostructural

Electrocatalyst for Water Splitting. *ACS Appl. Mater. Interfaces* **2023**, *15* (29), 34682–34697. https://doi.org/10.1021/acsami.3c03021.

(30) Akbar, S.; Anwar, A.; Kanwal, Q. Electrochemical Determination of Folic Acid: A Short Review. *Anal. Biochem.* **2016**, *510*, 98–105. https://doi.org/10.1016/j.ab.2016.07.002.

(31) Rana, S.; Shetake, N. G.; Barick, K. C.; Pandey, B. N.; Salunke, H. G.; Hassan, P. A. Folic Acid Conjugated Fe3O4 Magnetic Nanoparticles for Targeted Delivery of Doxorubicin. *Dalt. Trans.* **2016**, *45* (43), 17401–17408. https://doi.org/10.1039/C6DT03323G.

(32) Chattopadhyay, S.; Dash, S. K.; Ghosh, T.; Das, D.; Pramanik, P.; Roy, S. Surface Modification of Cobalt Oxide Nanoparticles Using Phosphonomethyl Iminodiacetic Acid Followed by Folic Acid: A Biocompatible Vehicle for Targeted Anticancer Drug Delivery. *Cancer Nanotechnol.* **2013**, *4* (4–5), 103–116. https://doi.org/10.1007/s12645-013-0042-7.

(33) Abramova, A. M.; Kokorina, A. A.; Sindeeva, O. A.; Jolibois, F.; Puech, P.; Sukhorukov, G. B.; Goryacheva, I. Y.; Sapelkin, A. V. Molecular Nature of Breakdown of the Folic Acid under Hydrothermal Treatment: A Combined Experimental and DFT Study. *Sci. Rep.* **2020**, *10* (1), 19668. https://doi.org/10.1038/s41598-020-76311-y.

(34) Chekin, F.; Teodorescu, F.; Coffinier, Y.; Pan, G.-H.; Barras, A.; Boukherroub, R.; Szunerits, S. MoS2/Reduced Graphene Oxide as Active Hybrid Material for the Electrochemical Detection of Folic Acid in Human Serum. *Biosens. Bioelectron.* **2016**, *85*, 807–813. https://doi.org/https://doi.org/10.1016/j.bios.2016.05.095.

(35) Sun, Y.; Wang, X.; Zhang, H. Sensitive and Stable Electrochemical Sensor for Folic Acid Determination Using a ZIF-67/AgNWs Nanocomposite. *Biosensors* **2022**, *12* (6). https://doi.org/10.3390/bios12060382.

(36) *Handbook of Nanobioelectrochemistry*; 2023. https://doi.org/10.1007/978-981-19-9437-1.

(37) Wang, K.; Li, Z. Y.; Peng, Y.; Zheng, T. F.; Chen, J. L.; Liu, S. J.; Wen, H. R. Highly Stable Rare Earth Metal-Organic Frameworks for Fluorescence Recognition of Folic Acid, Proton Conduction, and Magnetic Refrigeration. *Inorg. Chem.* **2023**, *62* (43), 17993–18001. https://doi.org/10.1021/acs.inorgchem.3c03034.

(38) Mohammadi, S. Z.; Mousazadeh, F.; Mohammadhasani-Pour, M. Electrochemical Detection of Folic Acid Using a Modified Screen Printed Electrode. *J. Electrochem. Sci. Eng.* **2022**, *12* (6), 1111–1120. https://doi.org/10.5599/jese.1360.

(39) Aflatoonian, M. R.; Tajik, S.; Ekrami-Kakhki, M. S.; Aflatoonian, B.; Beitollahi, H. A Nano-Sensor Based on Screen Printed Electrode (SPE) for Electro-Chemical

Detection of Vitamin B9. *Eurasian Chem. Commun.* **2020**, *2* (5), 609–618. https://doi.org/10.33945/SAMI/ECC.2020.5.7.

(40) Li, D.; Jia, Y.; Li, Z.; Liu, L.; Wu, N.; Hu, M. Identification of Folic Acid and Sulfaquinoxaline Using a Heterometallic Zn-Eu MOF as a Sensor. *Dalt. Trans.* **2022**, *52* (3), 696–702. https://doi.org/10.1039/d2dt03446h.

(41) Quan, X.; Yan, B. In Situ Generated Dye@MOF/COF Heterostructure for Fluorescence Detection of Chloroquine Phosphate and Folic Acid via Different Luminescent Channels. *ACS Appl. Mater. Interfaces* **2023**, *15* (47), 54634–54642. https://doi.org/10.1021/acsami.3c11298.

(42) Yang, B.; Li, X.; Wang, L.; An, J.; Wang, T.; Zhang, F.; Ding, B.; Li, Y. A Water-Stable MOF-AgClO4-Abtz as Fluorescent Sensor for Detection of Folic Acid Based on Inner Filter Effect. *Talanta* **2020**, *217*, 121019. https://doi.org/https://doi.org/10.1016/j.talanta.2020.121019.

(43) Hasan, I. M. A.; Abd-Elsabur, K. M.; Assaf, F. H.; Abd-Elsabour, M. Folic Acid Determination in Food Samples Using Green Synthesized Copper Oxide Nanoparticles and Electro-Poly (Methyl Orange) Sensor. *Electrocatalysis* **2022**, *13* (6), 759–772. https://doi.org/10.1007/s12678-022-00756-0.

(44) Ganesh, P. S.; Kim, S. Y.; Choi, D. S.; Kaya, S.; Serdaroğlu, G.; Shimoga, G.; Shin, E. J.; Lee, S. H. Electrochemical Investigations and Theoretical Studies of Biocompatible Niacin-Modified Carbon Paste Electrode Interface for Electrochemical Sensing of Folic Acid. *J. Anal. Sci. Technol.* **2021**, *12* (1). https://doi.org/10.1186/s40543-021-00301-6.

(45) Mani, V.; Balamurugan, T. S. T.; Huang, S. T. Rapid One-Pot Synthesis of Polydopamine Encapsulated Carbon Anchored with Au Nanoparticles: Versatile Electrocatalysts for Chloramphenicol and Folic Acid Sensors. *Int. J. Mol. Sci.* **2020**, *21* (8). https://doi.org/10.3390/ijms21082853.

(46) Yuan, M. M.; Zou, J.; Huang, Z. N.; Peng, D. M.; Yu, J. G. PtNPs-GNPs-MWCNTs-β-CD Nanocomposite Modified Glassy Carbon Electrode for Sensitive Electrochemical Detection of Folic Acid. *Anal. Bioanal. Chem.* **2020**, *412* (11), 2551–2564. https://doi.org/10.1007/s00216-020-02488-w.

(47) Movileanu, C.; Anghelache, M.; Turtoi, M.; Voicu, G.; Neacsu, I. A.; Ficai, D.; Trusca, R.; Oprea, O.; Ficai, A.; Andronescu, E.; Calin, M. Folic Acid-Decorated PEGylated Magnetite Nanoparticles as Efficient Drug Carriers to Tumor Cells Overexpressing Folic Acid Receptor. *Int. J. Pharm.* **2022**, *625*, 122064. https://doi.org/https://doi.org/10.1016/j.ijpharm.2022.122064.

(48) Dong, S.; Cho, H. J.; Lee, Y. W.; Roman, M. Synthesis and Cellular Uptake of Folic Acid-Conjugated Cellulose Nanocrystals for Cancer Targeting. *Biomacromolecules* **2014**, *15* (5), 1560–1567. https://doi.org/10.1021/bm401593n.

ଔ